A Linear Theory for Periodic Convectively Forced Gravity Waves near a Coastline

YU DU,[a,b,c] RICHARD ROTUNNO,[d] ZIJIAN CHEN,[a] AND HONGPEI YANG[a]

[a] *School of Atmospheric Sciences, Sun Yat-sen University, and Southern Marine Science and Engineering Guangdong Laboratory (Zhuhai), Zhuhai, China*
[b] *Guangdong Province Key Laboratory for Climate Change and Natural Disaster Studies, Sun Yat-sen University, Zhuhai, China*
[c] *Key Laboratory of Tropical Atmosphere-Ocean System, Sun Yat-sen University, Ministry of Education, Zhuhai, China*
[d] *National Science Foundation, National Center for Atmospheric Research, Boulder, Colorado*

(Manuscript received 25 September 2023, in final form 24 March 2024, accepted 6 April 2024)

ABSTRACT: This study presents a simple 2D linear analytical model aimed at investigating gravity waves forced by temporally periodic convection near a coastline. This investigation encompasses two distinct convective heating scenarios: deep convective heating and stratiform heating/cooling. Our model explores the intricate behavior of gravity waves in proximity to a time-dependent convective source and examines their propagation characteristics across diverse atmospheric conditions. Close to the convective source, gravity waves demonstrate nearly horizontal propagation with vertically aligned phase lines. The velocity of their propagation primarily depends on the vertical scale of the convective heating. The presence of a tropopause further extends their horizontal reach through partial wave ducting between the surface and the tropopause. However, the horizontal scale of the convective heating also plays a crucial role in determining the horizontal wavelength and, consequently, affecting the horizontal propagation speed of the gravity waves. If the heating horizontal scale is small compared to the horizontal scale of free waves at the forcing frequency, the heating vertical scale determines the vertical wavelength and thus the horizontal wavelength. However, if the heating horizontal scale is large, the horizontal wavelength determined by the heating vertical scale has little energy, so that the horizontal wavelength is mainly determined by the heating horizontal scale. Moreover, longer periods of convective heating and stronger background winds contribute to an increased downstream propagation distance of the gravity waves away from the source. Additionally, inertia–gravity waves generated by diurnal convection can propagate horizontally over greater distances at a higher latitude but become confined or trapped at latitudes exceeding 30°.

KEYWORDS: Convection; Gravity waves; Heating

1. Introduction

Convection plays a significant role in generating gravity waves, and conversely, gravity waves also serve as a mechanism for triggering and organizing convection (Shige and Satomura 2001; Tulich and Mapes 2008; Lane and Zhang 2011; Su and Zhai 2017; Wilson et al. 2018; Du and Zhang 2019). By modifying the cloud environment and supplying uplift (Lane and Reeder 2001; Fovell et al. 2006; Adams-Selin 2020; Yang and Du 2024), gravity waves may subsequently influence convection. Beyond that, convectively forced gravity waves may also help shaping the momentum budget of the middle atmosphere, contributing to the general circulation (Fritts and Alexander 2003; Stephan et al. 2021).

Convectively generated gravity waves represent the atmospheric response to the distinctive heating profiles found within convective systems, encompassing both convective and stratiform regions (Pandya et al. 2000). In convective regions, the heating profile displays warming throughout the tropospheric depth, with a peak at the midlevel. In contrast, a stratiform region is characterized by upper-level warming and lower-level cooling (Houze 1982; Gallus and Johnson 1991). Arising from the distinctive convective activities in these two regions, the discrepancies in heating profiles can contribute significantly to the generation of distinct wave modes (Lane 2015). Moreover, nonlinear mechanical forcing has also been proposed to play a role in generating gravity waves (Fritts and Alexander 2003; Song et al. 2003; Yang et al. 2023).

Nicholls et al. (1991) established a linear two-dimensional model to probe the forced gravity wave response to prescribed steady or transient heat sources. Their investigation showed that the response is in the form of an internal gravity wave propagating horizontally away from the source, characterized by a velocity that depends on the vertical wavelength of the heating within either a rigid-lid or semi-infinite setting. Specifically, the $n = 1$ mode, defined by half its vertical wavelength equal to the tropospheric depth (also the heating depth), exhibited deep and fast movement. Conversely, the $n = 2$ mode, with a vertical wavelength equal to the tropospheric depth, displayed a slower horizontal propagation, linked to opposite vertical motions in the lower and upper troposphere. Pandya et al. (1993) argued that in the semi-infinite scenario, the wave response in a uniformly stratified atmosphere would be significantly weaker compared to it in the rigid-lid scenario, as energy could disperse through vertically propagating gravity waves. Halliday et al. (2018) extended the theory of Nicholls et al. (1991) by incorporating a jump in the Brunt–Väisälä frequency to include the influence of the tropopause for both steady and transient heat sources. The tropopause, serving as an imperfect reflective surface, was identified as an important factor in wave energy confinement.

Corresponding author: Yu Du, duyu7@mail.sysu.edu.cn

DOI: 10.1175/JAS-D-23-0173.1

© 2024 American Meteorological Society. This published article is licensed under the terms of the default AMS reuse license. For information regarding reuse of this content and general copyright information, consult the AMS Copyright Policy (www.ametsoc.org/PUBSReuseLicenses).

Authenticated duyu7@mail.sysu.edu.cn | Downloaded 07/31/24 01:46 AM UTC

Considering that short-lived and long-lived convection manifest distinct periods within their respective convective life cycles, there emerge diverse frequency peaks in the cloud power spectrum, spanning intervals from days to hours, and even minutes (Alexander et al. 1995; Lane and Zhang 2011). Hence, it is desirable to ascertain the gravity wave response to heat sources with different periods. Recent work by Short et al. (2023) introduced a linear analytic theory elucidating diurnally forced gravity waves originating from upper-tropospheric convective heating associated with a diurnally recurring convective line at the coastline. Gravity waves excited by convection on land serve as an important mechanism for offshore diurnal rainfall propagation (Love et al. 2011; Hassim et al. 2016; Fang and Du 2022). However, in addition to the diurnal cycle, convection exhibits its own inherent periodic heat sources owing to its life cycle.

The present study builds upon previous work on waves emitted by a heating source (Beres 2004, 2005; Song and Chun 2005; Song et al. 2007) in several respects. In particular, Beres (2004) considered constant Brunt–Väisälä frequency N (no tropopause), Song and Chun (2005) considered varying N (with tropopause) under the hydrostatic approximation, and both models neglect the Coriolis force. The present model includes varying N, nonhydrostatic dynamics, and the Coriolis force. Also, we use linear damping to ensure the decay of the wave solutions away from the heating source which avoids the explicit consideration of radiation conditions, and using Green's function, our approach can accommodate more complex heating functions. While Beres (2004) and Song and Chun (2005) focus on vertical wave momentum flux from a horizontally localized source, the present paper is concerned with the offshore horizontal propagation resulting from convection over a wide area (land). Finally, these previous studies predominantly focused on deep vertical heating profiles [e.g., $\sin(n\pi/H)$ with $n = 1$, where H is the height of the tropopause]; the present study, motivated by the physics of precipitating convection, compares cases with $n = 1$ and $n = 2$.

The organization of the paper is as follows. Section 2 introduces the development of a two-dimensional linear analytical model for periodic thermally forced gravity waves excited by convection, accounting for distinct stability layers corresponding to the troposphere and stratosphere. Section 3 compares the characteristics of $n = 1$ and $n = 2$ gravity waves while examining the influence of the tropopause on wave propagation. Section 4 delves into the impacts of the horizontal scale and period of convection, background wind, and latitude on the gravity waves' response. Finally, in section 5, we summarize our findings and present our concluding remarks.

2. Linear analytical model

a. Linear equations and nondimensional analysis

Two-dimensional linear equations of motion under the Boussinesq approximation accounting for background wind and friction can be written as follows (Rotunno 1983; Qian et al. 2009; Du and Rotunno 2015, 2018; Short et al. 2023):

$$\left(\frac{\partial}{\partial t^*} + U^*\frac{\partial}{\partial x^*}\right)u^* - f^*v^* = -\frac{\partial P^*}{\partial x^*} - \alpha^* u^*, \tag{1}$$

$$\left(\frac{\partial}{\partial t^*} + U^*\frac{\partial}{\partial x^*}\right)v^* + f^*u^* = -\alpha^* v^*, \tag{2}$$

$$\left(\frac{\partial}{\partial t^*} + U^*\frac{\partial}{\partial x^*}\right)w^* - b^* = -\frac{\partial P^*}{\partial z^*} - \alpha^* w^*, \tag{3}$$

$$\left(\frac{\partial}{\partial t^*} + U^*\frac{\partial}{\partial x^*}\right)b^* + N^{*2}w^* = Q^* - \alpha^* b^*, \tag{4}$$

$$\frac{\partial u^*}{\partial x^*} + \frac{\partial w^*}{\partial z^*} = 0, \tag{5}$$

where U^* represents the uniform background wind in the x^* direction, (u^*, v^*, w^*) refer to the velocity perturbations in the (x^*, y^*, z^*) directions, f^* is the Coriolis parameter, b^* is the buoyancy, and P^* is the Boussinesq disturbance pressure variable. The frictional damping is included as $-(\alpha^* u^*, \alpha^* v^*, \alpha^* w^*)$, with α^* representing the friction coefficient (s^{-1}). The inclusion of the linearized friction term in this study serves the primary purpose of ensuring exponential decay away from the heating source and avoids the explicit consideration of radiation conditions; the parameter α^* is assigned a small value (10^{-11} s^{-1}) to achieve this objective.[1] The convective heating function (Fig. 1) is specified as follows:

$$Q^* = \begin{cases} \dfrac{Q_0}{\pi}\left(\dfrac{\pi}{2} - \arctan\dfrac{x^*}{x_0^*}\right)\sin\left(\dfrac{n\pi z^*}{H}\right)e^{-i\omega t^*} & \text{when } z^* < H \\ 0 & \text{when } z^* \geq H \end{cases}, \tag{6}$$

where Q_0 is the heating amplitude (1.2×10^{-5} m s^{-3}), H is the heating/tropopause height (10 km), and $\omega = 2\pi/T$, where $T = 2$ h is the period of convective heating. In this study, the arctangent-shaped heat source is used to reproduce convection over a broad area (land). The convective heating is situated on the negative x^* side, decaying horizontally at $x^* = 0$ with a scale of x_0^* that represents the horizontal scale of convection. We compared the arctangent-shaped source with the Gaussian-shaped source, and their gravity wave propagation patterns are generally consistent, as we will show later. Our focus is on the wave response forced by convection on the positive x^* side. Vertically, the sine wave structure below the tropopause corresponds to deep convection (the first mode when $n = 1$) and stratiform conditions (the second mode when $n = 2$).[2] No convective heating is present above the tropopause. The N^* represents the buoyancy frequency, with $N_1^* = 0.01\,s^{-1}$ in the troposphere ($z^* < H$) and $N_2^* = 0.01$ or $0.02\,s^{-1}$ in the stratosphere ($z^* \geq H$).

Next, the nondimensional dependent variables are defined as follows:

[1] An additional experiment was conducted with a 10 times larger value of control α^* (10^{-10} s^{-1}), and their results demonstrate consistency, supporting the chosen small value of α^* is adequate.

[2] Practically, we set $n = -2$ to specify lower cooling and upper warming.

Authenticated duyu7@mail.sysu.edu.cn | Downloaded 07/31/24 01:46 AM UTC

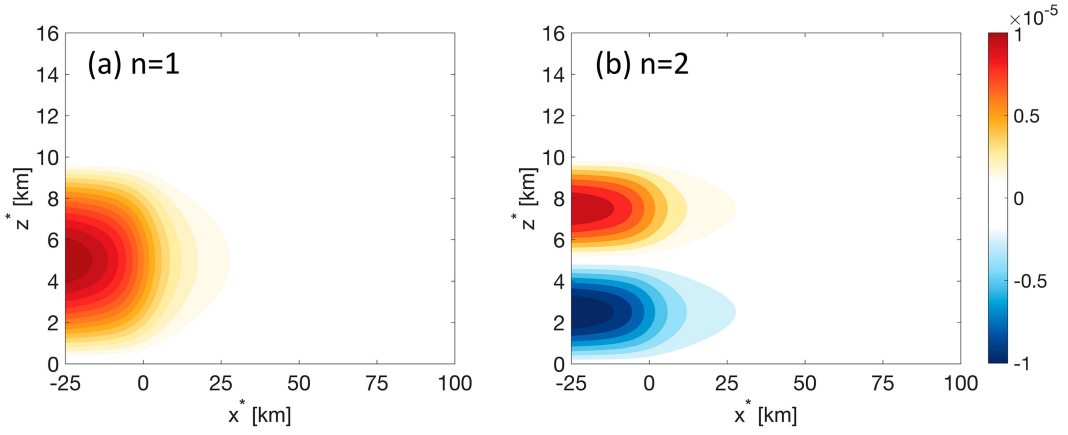

FIG. 1. The heating function Q^* (m s^{-3}) given by (6) for (a) the first mode ($n = 1$) and (b) the second mode ($n = 2$) at $t = 0$, with $Q_0 = 1.2 \times 10^{-5}$ m s^{-3}, $x_0^* = 10$ km, and $H = 10$ km.

$$\begin{aligned} &x^* = Hx, \quad && z^* = Hz, \quad && t^* = \frac{t}{\omega}, \quad && (u^*, v^*, w^*) = H\omega(u, v, w), \\ &b^* = H\omega^2 b, \quad && P^* = H^2\omega^2 P, \quad && f^* = \omega f, \quad && \alpha^* = \omega\alpha, \\ &Q^* = H\omega^3 Q, \quad && U^* = H\omega U, \quad && N^* = \omega N, \quad && x_0^* = Hx_0 . \end{aligned} \tag{7}$$

Rewriting (1)–(5) based on the above nondimensional variables, we obtain

$$\left(\frac{\partial}{\partial t} + U\frac{\partial}{\partial x} + \alpha\right)u - fv = -\frac{\partial P}{\partial x}, \tag{8}$$

$$\left(\frac{\partial}{\partial t} + U\frac{\partial}{\partial x} + \alpha\right)v + fu = 0, \tag{9}$$

$$\left(\frac{\partial}{\partial t} + U\frac{\partial}{\partial x} + \alpha\right)w - b = -\frac{\partial P}{\partial z}, \tag{10}$$

$$\left(\frac{\partial}{\partial t} + U\frac{\partial}{\partial x} + \alpha\right)b + N^2 w = Q, \tag{11}$$

$$\frac{\partial u}{\partial x} + \frac{\partial w}{\partial z} = 0. \tag{12}$$

b. *The analytical solution*

Equations (8)–(12) can be combined into a single equation for the streamfunction $\psi(u = \partial\psi/\partial z, w = -\partial\psi/\partial x)$:

$$\left[\left(\frac{\partial}{\partial t} + U\frac{\partial}{\partial x} + \alpha\right)^2 + f^2\right]\frac{\partial^2\psi}{\partial z^2} + \left[N^2 + \left(\frac{\partial}{\partial t} + U\frac{\partial}{\partial x} + \alpha\right)^2\right]\frac{\partial^2\psi}{\partial x^2} = -\frac{\partial Q}{\partial x}. \tag{13}$$

With $Q = [Q_0/(\pi H\omega^3)][(\pi/2) - \arctan(x/x_0)]\sin(n\pi z)e^{-it}$ and $\psi \propto \tilde{\psi}e^{-it}$, (13) can be simplified as follows:

$$\begin{aligned} &\left[\left(-i + U\frac{\partial}{\partial x} + \alpha\right)^2 + f^2\right]\frac{\partial^2\tilde{\psi}}{\partial z^2} + \left[N^2 + \left(-i + U\frac{\partial}{\partial x} + \alpha\right)^2\right]\frac{\partial^2\tilde{\psi}}{\partial x^2} = \frac{Q_0}{\pi H\omega^3}\frac{x_0}{x_0^2 + x^2}\sin(n\pi z) \quad \text{for } z < 1 \\ &\left[\left(-i + U\frac{\partial}{\partial x} + \alpha\right)^2 + f^2\right]\frac{\partial^2\tilde{\psi}}{\partial z^2} + \left[N^2 + \left(-i + U\frac{\partial}{\partial x} + \alpha\right)^2\right]\frac{\partial^2\tilde{\psi}}{\partial x^2} = 0 \qquad\qquad \text{for } z > 1 \end{aligned} . \tag{14}$$

Applying the Fourier transform to (14) in the x direction using $\hat{\psi} = \int_{-\infty}^{\infty}\tilde{\psi}e^{-iKx}dx$ and introducing $\sigma = 1 - KU + i\alpha = \sigma_r + i\alpha$, (14) becomes

$$\begin{aligned} &(f^2 - \sigma^2)\frac{\partial^2\hat{\psi}}{\partial z^2} - (N^2 - \sigma^2)K^2\hat{\psi} = \frac{Q_0}{H\omega^3}e^{-x_0|K|}\sin(n\pi z) \quad \text{for } z < 1 \\ &(f^2 - \sigma^2)\frac{\partial^2\hat{\psi}}{\partial z^2} - (N^2 - \sigma^2)K^2\hat{\psi} = 0 \qquad\qquad\qquad\qquad\quad \text{for } z > 1 \end{aligned} . \tag{15}$$

Authenticated duyu7@mail.sysu.edu.cn | Downloaded 07/31/24 01:46 AM UTC

Let γ be defined as $\gamma = \sqrt{[(N^2 - \sigma^2)K^2]/(f^2 - \sigma^2)} \cong \sqrt{[(N^2 - \sigma_r^2)/(f^2 - \sigma_r^2)]K^2 + i[2\alpha\sigma_r(N^2 - f^2)/(f^2 - \sigma_r^2)^2]K^2} \cong \sqrt{[(N^2 - \sigma_r^2)/(f^2 - \sigma_r^2)]K^2 + i[2\alpha\sigma_r N^2/(f^2 - \sigma_r^2)^2]K^2}$ when $\alpha \ll 1$, $N^2 \gg f^2$. Hence, γ is a complex number and can be further expressed as follows:

$$\gamma \cong \sqrt{\mathcal{A} + i\mathcal{B}} = \begin{cases} \sqrt{\dfrac{\sqrt{\mathcal{A}^2 + \mathcal{B}^2} + \mathcal{A}}{2}} + i\sqrt{\dfrac{\sqrt{\mathcal{A}^2 + \mathcal{B}^2} - \mathcal{A}}{2}} & \text{for } \mathcal{B} > 0 \\ \sqrt{\dfrac{\sqrt{\mathcal{A}^2 + \mathcal{B}^2} + \mathcal{A}}{2}} - i\sqrt{\dfrac{\sqrt{\mathcal{A}^2 + \mathcal{B}^2} - \mathcal{A}}{2}} & \text{for } \mathcal{B} < 0 \end{cases}, \tag{16}$$

where

$$\mathcal{A} = \frac{N^2 - \sigma_r^2}{f^2 - \sigma_r^2}K^2, \quad \mathcal{B} = \frac{2\alpha\sigma_r N^2}{(f^2 - \sigma_r^2)^2}K^2.$$

For σ_r $(=1 - KU) > 0$, $\mathcal{B} > 0$ and the first member of (16) applies. If in addition $f^2 < \sigma_r^2 < N^2$, $\mathcal{A} < 0$, $|\mathcal{B}| \ll |\mathcal{A}|$, then $\sqrt{(\sqrt{\mathcal{A}^2 + \mathcal{B}^2} + \mathcal{A})/2} \cong \sqrt{(|\mathcal{A}|\{1 + [\mathcal{B}^2/(2\mathcal{A}^2)]\} + \mathcal{A})/2} = |\mathcal{B}|/(2\sqrt{|\mathcal{A}|})$ and $\sqrt{(\sqrt{\mathcal{A}^2 + \mathcal{B}^2} - \mathcal{A})/2} \cong \sqrt{|\mathcal{A}|}$ so that

$$\gamma \cong \left|\frac{\alpha\sigma_r N^2}{(f^2 - \sigma_r^2)^2}\right|\sqrt{\left|\frac{f^2 - \sigma_r^2}{N^2 - \sigma_r^2}\right|}K + i\sqrt{\left|\frac{N^2 - \sigma_r^2}{f^2 - \sigma_r^2}\right|}K^2. \tag{17}$$

For $\sigma_r < 0$, $\mathcal{B} < 0$ and the second member of (16) applies. If in addition $f^2 < \sigma_r^2 < N^2$ and $\mathcal{A} < 0$ then

$$\gamma \cong \left|\frac{\alpha\sigma_r N^2}{(f^2 - \sigma_r^2)^2}\right|\sqrt{\left|\frac{f^2 - \sigma_r^2}{N^2 - \sigma_r^2}\right|}K - i\sqrt{\left|\frac{N^2 - \sigma_r^2}{f^2 - \sigma_r^2}\right|}K^2. \tag{18}$$

Finally, if $\sigma_r^2 > N^2 > f^2$ and $\mathcal{A} > 0$, then

$$\gamma \cong \sqrt{\left|\frac{N^2 - \sigma_r^2}{f^2 - \sigma_r^2}\right|}K^2 + \mathrm{sgn}(\mathcal{B})i\left|\frac{\alpha\sigma_r N^2}{(f^2 - \sigma_r^2)^2}\right|\sqrt{\left|\frac{f^2 - \sigma_r^2}{N^2 - \sigma_r^2}\right|}K. \tag{19}$$

Equations (17)–(19) will be useful for interpretations given below.

Equation (15) is thus transformed into the following form:

$$\frac{\partial^2\hat{\psi}}{\partial z^2} - \gamma^2\hat{\psi} = \hat{F}, \tag{20}$$

where

$$\hat{F} = \begin{cases} \dfrac{Q_0}{H\omega^3(f^2 - \sigma^2)}e^{-x_0|K|}\sin(n\pi z) & \text{for } z < 1 \\ 0 & \text{for } z > 1 \end{cases}. \tag{21}$$

Following Rotunno (1983) and Short et al. (2023), (20) can be solved using Green's function. The Green's function equation for (20) is

$$\frac{\partial^2 G}{\partial z^2} - \gamma^2 G = \delta(z - z'), \tag{22}$$

where $G(z, z')$ is Green's function and δ is the Dirac delta function, representing a point source at z'. The solution for $G(z, z')$ becomes

$$G(z, z') = \begin{cases} A\sinh\gamma_1 z, & \text{for } z < z' < 1 \\ Be^{-\gamma_1(z-1)} + Ce^{\gamma_1(z-1)}, & \text{for } z' < z < 1 \\ De^{-\gamma_2(z-1)}, & \text{for } z' < 1 < z \end{cases}, \tag{23}$$

where $\gamma_1 = \sqrt{[(N_1^2 - \sigma^2)K^2]/(f^2 - \sigma^2)}$ and $\gamma_2 = \sqrt{[(N_2^2 - \sigma^2)K^2]/(f^2 - \sigma^2)}$. Green's function satisfies the lower boundary condition, $G(z = 0) = 0$, and remains finite as z approaches infinity. By enforcing the continuity of G and $\partial_z G$ at $z = 1$, we find $B + C = D$ and $-N_1 B + N_2 C = -N_2 D$, giving the reflection and refraction coefficient at the tropopause $(z = 1)$ as $C/B = (N_1 - N_2)/(N_1 + N_2)$ and $D/B = 2N_1/(N_1 + N_2)$, respectively (Lindzen and Tung 1976); with the latter formulas, we can express $B = [(N_1 + N_2)/(2N_1)]D$ and $C = [(N_1 - N_2)/(2N_1)]D$. Furthermore, the conditions on G at z' are

$$G(z'^+) = G(z'^-) \quad \text{and} \quad \partial_z G(z'^+) - \partial_z G(z'^-) = 1. \tag{24}$$

Consequently, we deduce that

$$A\sinh\gamma_1 z' = D\frac{N_1 + N_2}{2N_1}e^{-\gamma_1(z'-1)} + D\frac{N_1 - N_2}{2N_1}e^{\gamma_1(z'-1)}, \quad \text{and} \tag{25}$$

$$-\gamma_1 D\frac{N_1 + N_2}{2N_1}e^{-\gamma_1(z'-1)} + \gamma_1 D\frac{N_1 - N_2}{2N_1}e^{\gamma_1(z'-1)} - \gamma_1 A\cosh\gamma_1 z' = 1. \tag{26}$$

From (25) and (26), we obtain

$$A = -\frac{1}{\gamma_1 S}\left[\frac{N_1 + N_2}{2N_1}e^{-\gamma_1(z'-1)} + \frac{N_1 - N_2}{2N_1}e^{\gamma_1(z'-1)}\right], \tag{27}$$

$$D = -\frac{1}{\gamma_1 S}\sinh\gamma_1 z', \tag{28}$$

where $S = [(N_1 + N_2)/(2N_1)]e^{\gamma_1} + [(N_1 - N_2)/(2N_1)]e^{-\gamma_1}$. The solution of (14) using Green's function becomes

Authenticated duyu7@mail.sysu.edu.cn | Downloaded 07/31/24 01:46 AM UTC

$$\hat{\psi} = \left[\frac{N_1 + N_2}{2N_1} e^{-\gamma_1(z-1)} + \frac{N_1 - N_2}{2N_1} e^{\gamma_1(z-1)}\right] \times \int_0^z -\frac{1}{\gamma_1 S} \sinh\gamma_1 z' \hat{F} dz' + \sinh\gamma_1 z \times \int_z^1 -\frac{1}{\gamma_1 S}\left[\frac{N_1 + N_2}{2N_1} e^{-\gamma_1(z'-1)} + \frac{N_1 - N_2}{2N_1} e^{\gamma_1(z'-1)}\right] \hat{F} dz' \quad \text{for} \quad z < 1, \tag{29}$$

$$\hat{\psi} = e^{-\gamma_2(z-1)} \int_0^1 -\frac{1}{\gamma_1 S} \sinh\gamma_1 z' \hat{F} dz' \quad \text{for} \quad z > 1. \tag{30}$$

Using (21), (29) and (30) can be further simplified as follows:

$$\hat{\psi} = \begin{cases} \dfrac{Q_0 e^{-x_0|K|}}{H\omega^3(\sigma^2 - f^2)(\gamma_1^2 + \pi^2 n^2)} \left(\dfrac{-n\pi \cos n\pi}{\gamma_1 S} \sinh\gamma_1 z + \sin n\pi z\right), & \text{for } z < 1 \\ \dfrac{Q_0 e^{-x_0|K|}}{H\omega^3(\sigma^2 - f^2)(\gamma_1^2 + \pi^2 n^2)} \dfrac{-n\pi \cos n\pi}{\gamma_1 S} e^{-\gamma_2(z-1)} \sinh\gamma_1, & \text{for } z > 1 \end{cases}. \tag{31}$$

Applying the inverse Fourier transform, we obtain

$$\psi = \mathrm{Re}\left\{\frac{1}{2\pi}\int_{-\infty}^{\infty} \hat{\psi} e^{i(Kx-t)} dK\right\}, \tag{32}$$

$$u = \frac{\partial\psi}{\partial z} = \mathrm{Re}\left\{\frac{1}{2\pi}\int_{-\infty}^{\infty} \frac{\partial\hat{\psi}}{\partial z} e^{i(Kx-t)} dK\right\}, \tag{33}$$

$$w = -\frac{\partial\psi}{\partial x} = \mathrm{Re}\left\{\frac{-i}{2\pi}\int_{-\infty}^{\infty} \hat{\psi} K e^{i(Kx-t)} dK\right\}. \tag{34}$$

In this study, the integrations in (33) and (34) are numerically calculated using MATLAB.

3. Convectively generated gravity wave propagation with $f = 0$

To begin, we investigate the propagation of forced gravity waves induced by $n = 1$ convection at the equator ($f = 0$). Our analysis considers a simplified scenario with uniform background stability ($N_1^* = N_2^* = 0.01\ \mathrm{s}^{-1}$) and no background wind ($U = 0$). Figure 2 depicts the temporal evolution of the vertical velocity ($w^* = H\omega w$) and the horizontal velocity ($u^* = H\omega u$) in a vertical cross section.

Above the top of convection ($z^* > H = 10\,\mathrm{km}$ or $z > 1$), gravity waves extend infinitely far along ray paths that radiate upward and outward from the convective source. The phase lines exhibit a tilted structure, propagating downward and outward, with w and u in phase. According to (31)–(34), for $z > 1$, $u \sim -\gamma_2 e^{-\gamma_2(z-1)} = -i\sqrt{|N_2^2 - 1|K^2}\, e^{-i\sqrt{|N_2^2-1|K^2}(z-1)}$ and $w \sim -iKe^{-\gamma_2(z-1)} = -iKe^{-i\sqrt{|N_2^2-1|K^2}(z-1)}$, where $\gamma_2 \cong i\sqrt{|(N_2^2 - \sigma_r^2)/(f^2 - \sigma_r^2)|K^2} \cong i\sqrt{|N_2^2 - 1|K^2}$ when $\alpha \to 0$, $f = 0$, and $U = 0$ based on (17). These expressions for u and w illustrate their in-phase nature (w and p are also in phase) and the upward propagation of energy with a positive tilt.

In contrast, in the vicinity of the convective region below H, the phase lines are nearly vertical and the wave propagation is approximately horizontal, which implies w and u are nearly out of the phase. This polarization relationship resembles a trapped wave structure. According to (31)–(34), for $z < 1$, $u \sim (-\pi/s)\cosh\gamma_1 z + \pi\cos\pi z \cong (-\pi/s)\cos\sqrt{|N_1^2 - 1|K^2}z + \pi\cos\pi z$ and $w \sim -iK\{[-\pi/(\gamma_1 s)]\sinh\gamma_1 z + \sin\pi z\} \cong [i\pi/(\sqrt{|N_1^2 - 1|S})]\sin\sqrt{|N_1^2 - 1|K^2}z - iK\sin\pi z$, where $\gamma_1 \cong i\sqrt{|N_1^2 - 1|K^2}$ when $\alpha \to 0$, $f = 0$, and $U = 0$ based on (17). These expressions for u and w underscore their out-of-phase nature and the presence of a trapped wave structure, wherein both upward- and downward propagation waves coexist.

At $t^* = 0$ min (Fig. 2a), a downdraft (in response to the convection-produced updraft at $x^* < 0$) with its peak at $z^* = 5$ km is observed around $x^* = 25$ km. As time progresses, the downdraft moves to the right, reaching $x^* \approx 70$ km by $t^* = 40$ min (Fig. 2c). However, far from the convective region ($x^* > 100$ km) below H, the phase lines experience tilting, leading to w and u being in phase as the wave energy reflects off the surface and propagates upward. At 60 min, the wave updraft occurs near the convection and then propagates outward in a similar way (Figs. 2d–f).

We conducted a comparison of wave behaviors generated by the arctangent-shaped and Gaussian-shaped sources (Fig. 2 vs Fig. 3). The propagation patterns on the right side are generally consistent. The fundamental forcing driving these gravity waves is the horizontal gradient of heating, which remains similar for both heating sources.[3] A symmetric Gaussian-shaped source, akin to a wall at $x_0^* = 0$, generates waves propagating both leftward and rightward from each gradient zone. When the leftward-propagating wave from the right gradient zone meets the rightward-propagating wave from the left gradient zone, they meet at $x_0^* = 0$ at some altitude above the source, reflect when they meet, and then continue propagating upward, without affecting the low-level flow. In this study, our primary focus is on

[3] The maximum gradient is at $x^* = 0$ for the arctangent-shaped source, while for the Gaussian-shaped source, it is set at approximately $x^* = 20$ km.

Authenticated duyu7@mail.sysu.edu.cn | Downloaded 07/31/24 01:46 AM UTC

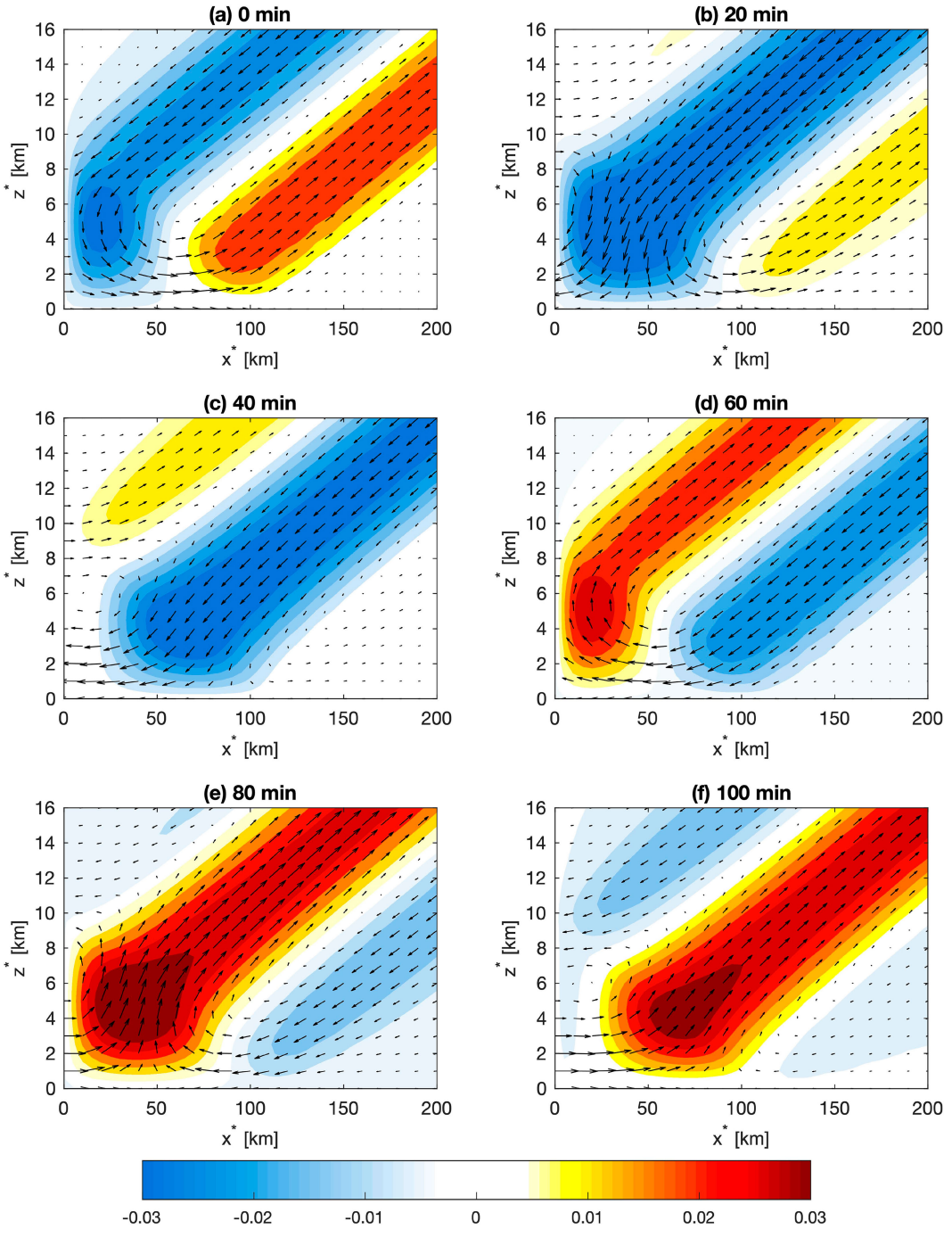

FIG. 2. Periodic evolution of the vertical cross section of vertical velocity (color shaded; m s^{-1}) and wind vectors (u^* and 10 w^*) forced by $n = 1$ mode convective heating with period $T = 2$ h and horizontal scale $x_0^* = 10$ km.

understanding the behavior of gravity waves induced by convection over a broad area. A practical scenario is the offshore propagation of gravity waves resulting from convection over the land (Love et al. 2011; Hassim et al. 2016); the arctangent-shaped source is used in the following discussion.

Furthermore, we explore here the influence of varying stability in the troposphere and stratosphere by setting $N_2^* = 2N_1^*$. Figures 4a and 4b illustrate a comparison of the gravity wave structures with and without a tropopause. In the presence of a tropopause, the phase lines above 10 km exhibit greater tilt away from the vertical compared to the case without a tropopause. The direction of wave energy propagation is governed by $\tan\theta = \mathrm{Im}(\gamma)/K = \sqrt{|(N^2 - \sigma_r^2)/(f^2 - \sigma_r^2)|} = \sqrt{(N^{*2}/\omega^2) - 1}$ for $N^{*2} \gg \omega^2$, where θ represents the angle of

Authenticated duyu7@mail.sysu.edu.cn | Downloaded 07/31/24 01:46 AM UTC

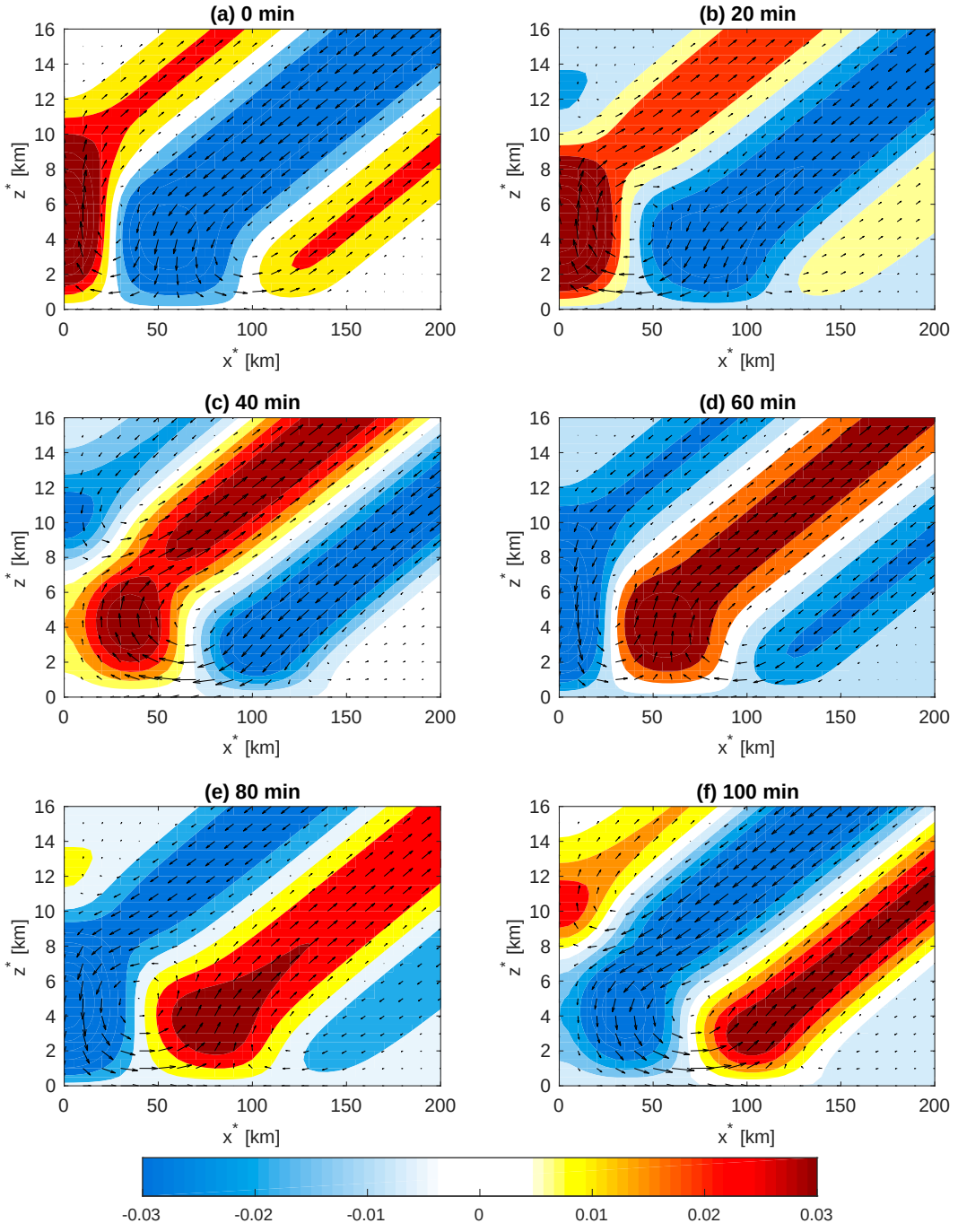

FIG. 3. As in Fig. 2, but for the Gaussian-shaped source $Q^* = Q_0 e^{-[x^{*2}/(2x_0^{*2})]} \sin(n\pi z^*/H) e^{-i\omega t^*}$ when $x_0^* = 20$ km.

energy propagation as measured from the vertical. As stability N^* doubles in the stratosphere, θ also increases. Below 10 km, the downdrafts near the source at $x^* = 25$ km in both cases exhibit similar characteristics. However, in the presence of a tropopause (Fig. 4b), the updraft at $x^* = \sim 120$ km shows stronger wave amplitude and a significant peak at $z^* = 5$ km due to wave reflection at the tropopause. In contrast, the case without the tropopause lacks such a maximum. The presence of a tropopause establishes a partial wave duct that promotes the horizontal propagation of gravity waves within the troposphere.

Next, we proceed to analyze gravity waves driven by $n = 2$ convection (Figs. 4c,d). Above 10 km, the phase lines tilt similarly to $n = 1$ waves, yet their vertical and horizontal wavelengths are smaller. The smaller imposed vertical wavelength ($n = 2$) requires a smaller horizontal wavelength since $\mathrm{Im}(\gamma)/K \cong N$, which is a fixed input. Below 10 km, $n = 2$ convection

Authenticated duyu7@mail.sysu.edu.cn | Downloaded 07/31/24 01:46 AM UTC

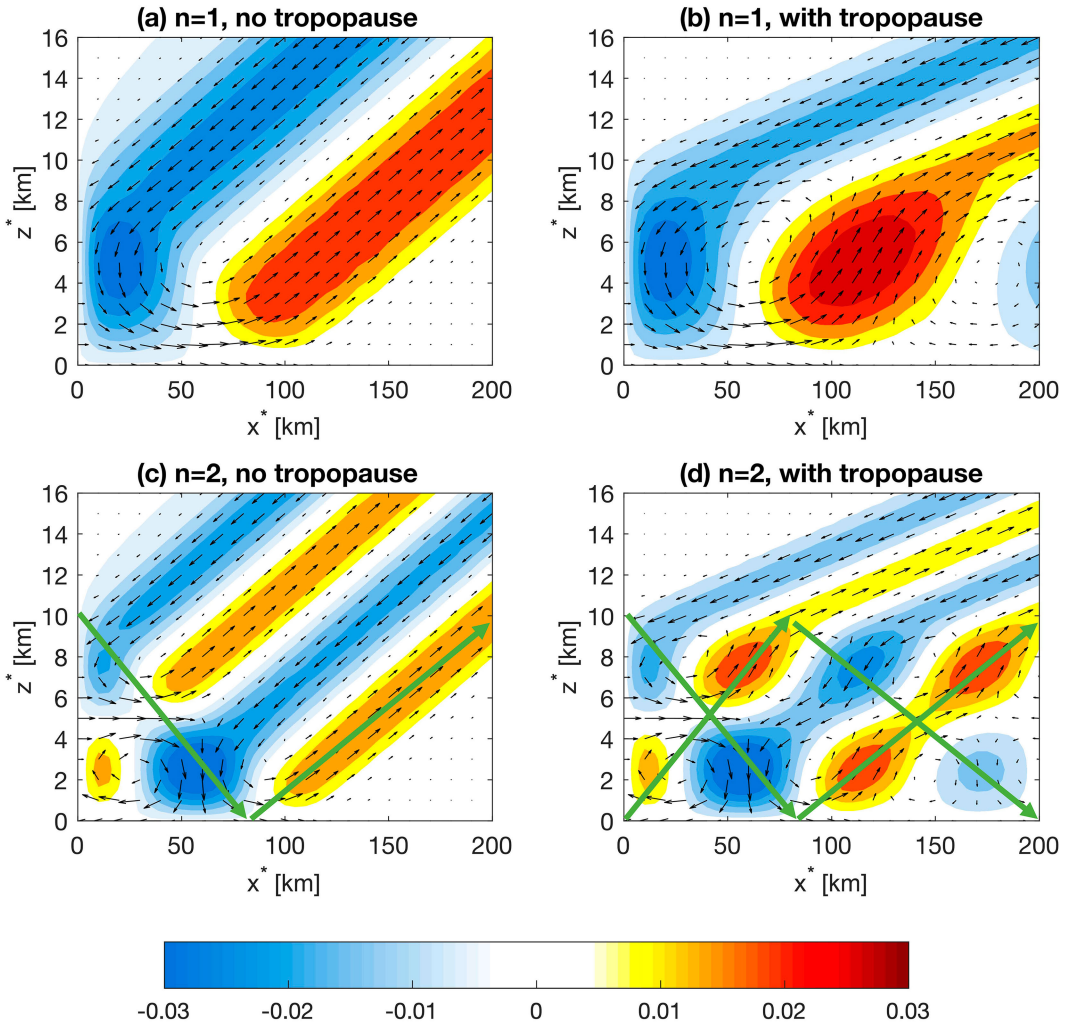

FIG. 4. As in Fig. 2a, but for (a) without a tropopause and (b) with a tropopause. (c),(d) As in (a) and (b), but for the $n = 2$ mode. The green vectors indicate the propagation and reflection of wave energy (group velocity).

generates downdraft–updraft couplets with peaks at $z^* = 2.5$ km and 7.5 km, which can propagate farther in the presence of a tropopause (Fig. 4d). A distinct reflection and interaction structure, known as wave ducting, is clearly observed between the tropopause and surface (green vectors in Fig. 4d), supporting long-distance horizontal propagation of gravity waves. In the absence of a tropopause, reflection occurs only at the surface (Fig. 4c).

To assess the horizontal propagation distances of gravity waves in different scenarios, Fig. 5 presents distance–time Hovmöller diagrams at constant heights depicting vertical motions. In Fig. 5a, vertical motions at $z^* = 5$ km for the $n = 1$ mode without a tropopause propagate periodically to the right (outward from the convection) until $x^* = 160$ km, with a velocity of 31.9 m s^{-1}. This velocity closely approximates what one would expect with a rigid lid. The theoretical speed calculated from the dispersion relationship is represented as $c = \omega/k^* = N^*H/(n\pi) = (0.01\,\mathrm{s}^{-1} \times 10\,\mathrm{km})/\pi = 31.8\,\mathrm{m\,s}^{-1}$. When $N_1^* \ll N_2^*$, the first term in (31) is small compared to the second term [$\sin n\pi z = \sin(n\pi z^*/H)$], which produces solutions closer to the case with a rigid lid (Nicholls et al. 1991). With the introduction of a tropopause, $n = 1$ gravity waves experience extended propagation (>250 km) while maintaining the same horizontal speed (Fig. 5b). The increased distance can be attributed to partial wave ducting between the surface and tropopause. Similarly, the $n = 2$ gravity waves demonstrate a comparable pattern of varying propagation distance with or without the tropopause (Figs. 5c,d) yet at a slower speed (15.9 m s^{-1}) due to the shorter vertical wavelength of $n = 2$ convection. This compares well with results using a rigid-lid tropopause, $c = N^*H/(n\pi) = (0.01\,\mathrm{s}^{-1} \times 10\,\mathrm{km})/2\pi = 15.9\,\mathrm{m\,s}^{-1}$.

4. Sensitivity of the gravity wave response to key parameters

a. The horizontal length scale of convective heating

The conventional choice for the horizontal length scale of convective heating, denoted as x_0^*, was set to 10 km in previous

Authenticated duyu7@mail.sysu.edu.cn | Downloaded 07/31/24 01:46 AM UTC

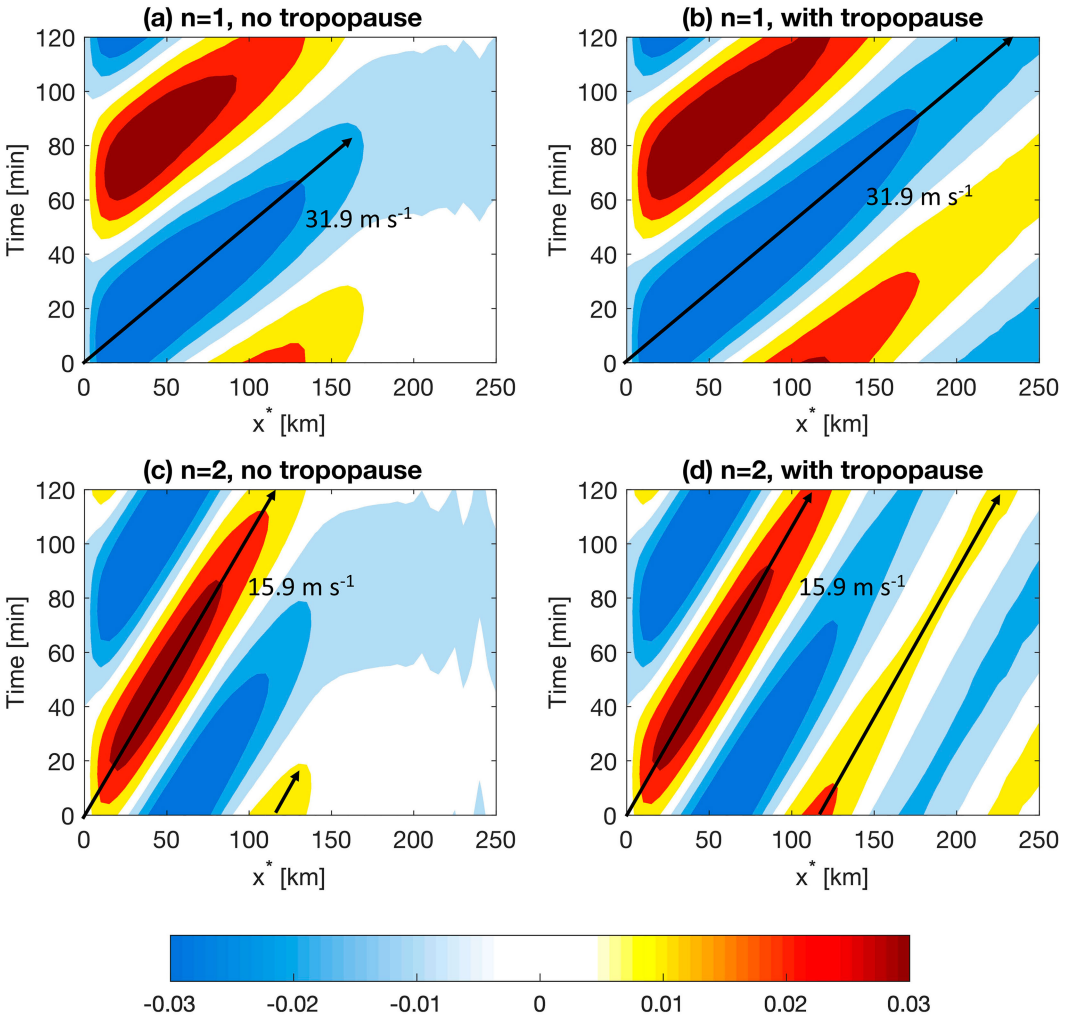

FIG. 5. Distance–time Hovmöller diagrams depicting the vertical motion (color shaded; m s^{-1}) at (a),(b) $z^* = 5$ km for the $n = 1$ convection and at (c),(d) $z^* = 2.5$ km for the $n = 2$ convection with period $T = 2$ h and horizontal scale $x_0^* = 10$ km. The absence of tropopause is indicated in (a) and (c), while tropopause is present in (b) and (d).

studies (Nicholls et al. 1991; Halliday et al. 2018), serving as a control parameter in this study (Fig. 1a). However, acknowledging the real-world variability in convective scale, ranging from single cells to mesoscale convective systems, it is important to assess the impact of x_0^* (5 and 50 km) on the gravity wave response in terms of their horizontal wavelengths and propagation speeds.

The $n = 1$ heating function structures (Figs. 6a,d) clearly demonstrate the smaller ($x_0^* = 5$ km) and larger ($x_0^* = 50$ km) horizontal scales of convection. When $x_0^* = 5$ km, the vertical structures of gravity waves with or without a tropopause (Figs. 6b,c) closely resemble those of the control case (Figs. 4a,b). Moreover, their horizontal propagation speeds and distances (Figs. 7a,b) exhibit similarities to the control case as well (Figs. 5a,b). These findings suggest that the horizontal scale of convection has limited influence on the horizontal wavelength and wave phase speed, which are primarily determined by the heating depth, consistent with Beres (2004).

However, substantial differences arise in the vertical structure of gravity waves when $x_0^* = 50$ km (Figs. 6e,f). In this case, the vertical scale is dominated by the first term in (31) since large x_0^* implies $K \ll 1$ and, therefore, $|\gamma_1| \ll 1$. In the absence of a tropopause (Fig. 6e), both the horizontal and vertical wavelengths increase compared to the control case or the $x_0^* = 5$ km case. The horizontal wave speed, $N/m = N\lambda_z/(2\pi)$, increases (46.1 m s^{-1}, Fig. 7c) since now the vertical wavelength is larger. In this scenario, the horizontal wavelength becomes less dependent on the vertical scale of the heating.

In contrast, the presence of a tropopause maintains the wave pattern at a considerable distance from the source, but notable differences in wave responses between $x_0^* = 5$ km and $x_0^* = 50$ km emerge near the source (Figs. 6c,f). For instance, near the source ($x < 50$ km), no maximum downward motion at $z = 5$ km is observed for the $x_0^* = 50$ km case (Figs. 6e,f) with or without a tropopause. Furthermore, the horizontal propagation speeds are larger near the source (43.3 m s^{-1})

Authenticated duyu7@mail.sysu.edu.cn | Downloaded 07/31/24 01:46 AM UTC

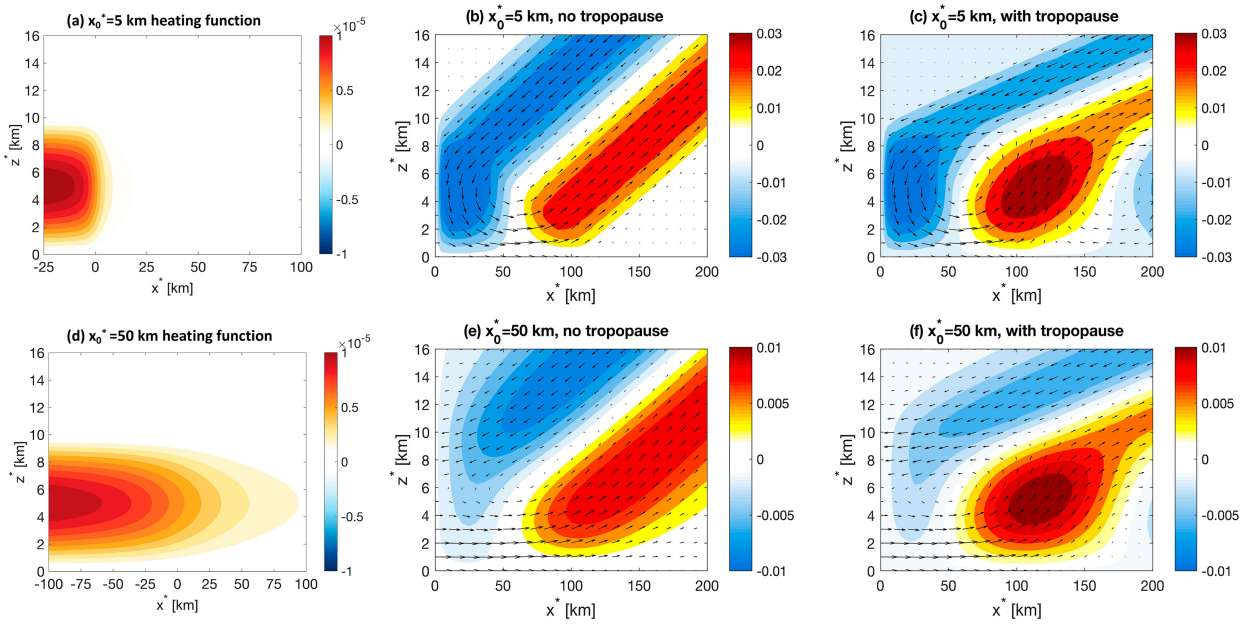

FIG. 6. As in Fig. 1a, but for (a) $x_0^* = 5$ km and (d) $x_0^* = 50$ km; as in Fig. 4a, but for (b) $x_0^* = 5$ km and (e) $x_0^* = 50$ km; as in Fig. 4b, but for (c) $x_0^* = 5$ km and (f) $x_0^* = 50$ km.

than the $x_0^* = 5$ km case but decrease away from the source (31.8 m s^{-1}), as depicted in Fig. 7d. The larger phase velocity near the source primarily results from the larger horizontal scale of the heating, whereas the lower phase velocity away from the source is predominantly affected by the presence of the partial ducting layer between the surface and tropopause, which is consistent with the speed for $x_0^* = 5$ km.

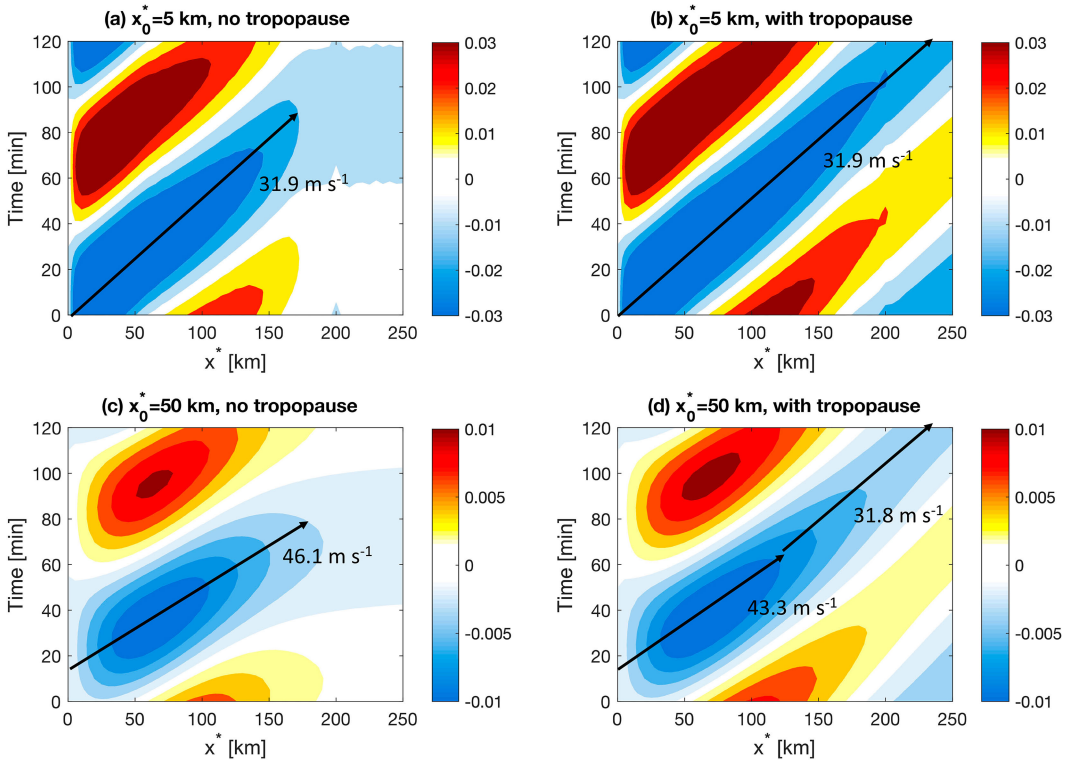

FIG. 7. As in Figs. 5a and 5b, but for (a),(b) $x_0^* = 5$ km and (c),(d) $x_0^* = 50$ km.

Authenticated duyu7@mail.sysu.edu.cn | Downloaded 07/31/24 01:46 AM UTC

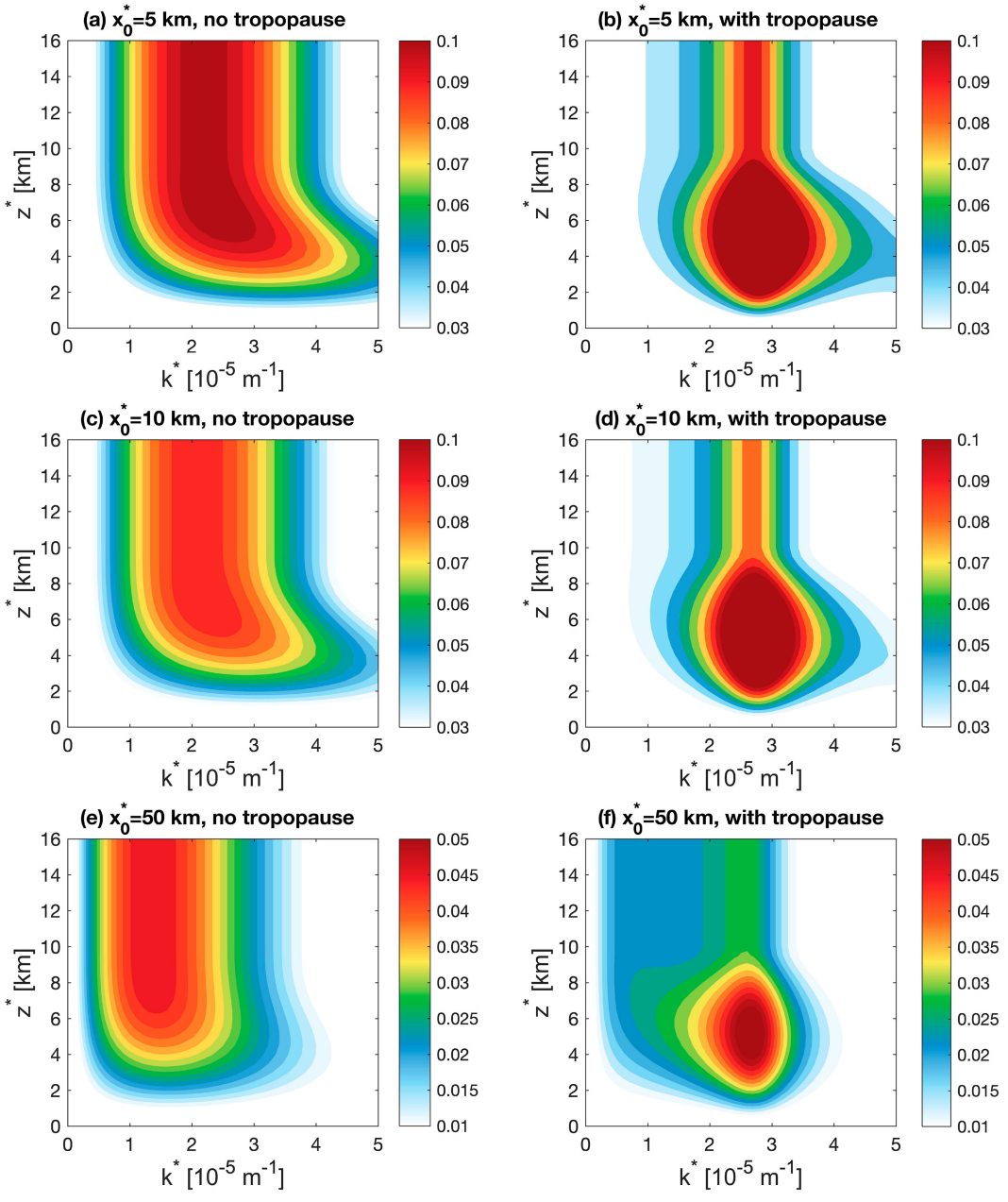

FIG. 8. The integrand $|-i\hat{\psi}K|$ plotted against $k^* = K/H$ (10^{-5} m^{-1}) and z^* (km) for (a),(b) $x_0^* = 5$ km; (c),(d) $x_0^* = 10$ km; and (e),(f) $x_0^* = 50$ km. The presence of tropopause is indicated in (b), (d), and (f), while no tropopause is present in (a), (c), and (e).

To understand the relation between the horizontal scale of convective heating and the horizontal wavelength of forced gravity waves, we begin by examining the analytical solution for w in (34). Figure 8 shows the wave amplitudes at different horizontal wavelengths, represented by the integrand $|-i\hat{\psi}K|$ as a function of wavenumber $k^* = k/H$. With the tropopause (Figs. 8b,d,f), the maximum amplitude occurs at $k^* = 2.75 \times 10^{-5}\text{m}^{-1}$ and an altitude of 5 km due to partial wave ducting between the surface and the tropopause. As in the dispersion relation for the $n = 1$ ducted waves, $k^* = \omega m/N^* = n\pi\omega/(N^*H) = 2.74 \times 10^{-5}\text{m}^{-1}$, corresponding to the maxima in Figs. 8b, 8d, and 8f. The dominant value of k^* is similar in the stratosphere and troposphere, owing to the upward energy propagation of gravity waves from the tropospheric source. Hence, the dominant horizontal wavelength remains unaffected by the horizontal scale of the heating when a tropopause is present.

Authenticated duyu7@mail.sysu.edu.cn | Downloaded 07/31/24 01:46 AM UTC

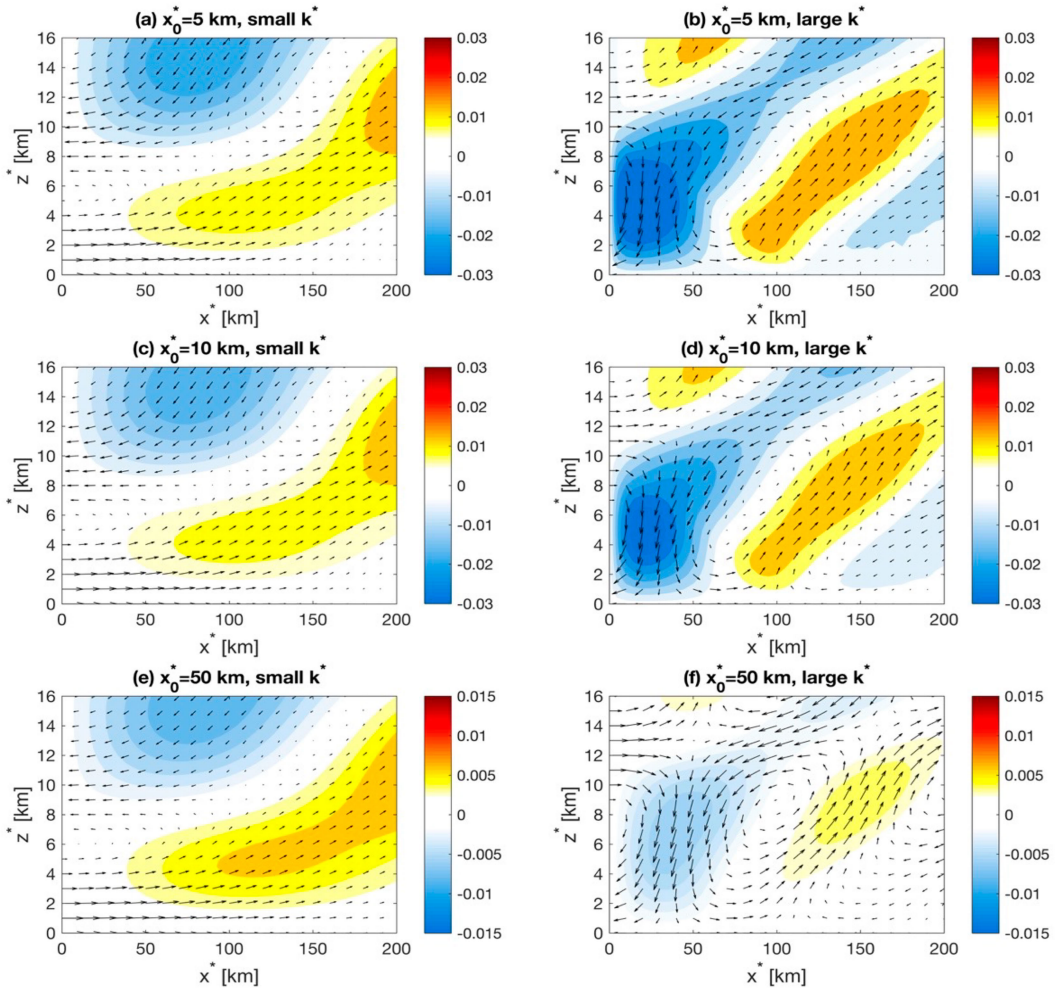

FIG. 9. As in Figs. 6b, 4a, and 6e, but for (a),(c),(e) $|k^*| < 2.5 \times 10^{-5}$ m^{-1} and (b),(d),(f) $|k^*| > 2.5 \times 10^{-5}$ m^{-1}.

On the other hand, in the absence of a tropopause (Figs. 8a,c,e), the maximum amplitude occurs at $k^* \cong 2.2 \times 10^{-5}$m^{-1} for a horizontal scale of heating $x_0^* = 5$ km or $x_0^* = 10$ km and at $k^* \cong 1.4 \times 10^{-5}$m^{-1} for $x_0^* = 50$ km. These peaks strongly correlate with the horizontal scale of the heating x_0. Additionally, in Figs. 8a and 8c, the maximum amplitude shifts to a higher value of k^* below $z = 10$ km (around 2.75×10^{-5} m^{-1} at 5-km altitude) due to the vertical scale of the heating ($n = 1$). Consequently, the predominant wave phase speed below 10-km altitude is primarily determined by the vertical scale of the heating. However, for $x_0^* = 50$ km, where wave energy is mainly confined to smaller k^* values, there is minimal energy present at larger k^* values such as 2.75×10^{-5} m^{-1} (Fig. 8e). Therefore, for large x_0^*, the dominant wave speed below 10-km altitude depends more on the horizontal scale of the heating than the vertical scale of the heating. Even in scenarios with both a tropopause and a large x_0^*, larger horizontal wavelengths are evident (Fig. 8f) compared to the case of a small x_0^* (Fig. 8a). Consequently, a faster propagation speed (43.3 m s^{-1} in Fig. 7d) due to a larger horizontal scale of heating is observed near the source.

Figure 9 provides deeper insight into the characteristics of gravity wave patterns with varying horizontal wavelengths in different x_0^* scenarios without a tropopause. The vertical structures of gravity waves with both large or small horizontal wavelengths for $x_0^* = 5$ km or 10 km closely resemble those for $x_0^* = 50$ km. However, notable disparities emerge in their relative wave amplitudes. Specifically, in the cases of $x_0^* = 5$ km and 10 km, the wave energy exhibits higher values for large k^* values ($|k^*| > 2.5 \times 10^{-5}$ m^{-1}) compared to smaller k^* values ($|k^*| < 2.5 \times 10^{-5}$ m^{-1}). Conversely, for $x_0^* = 50$ km, the wave energy associated with larger k^* values is significantly lower than that for smaller k^* values.

We further examine gravity wave patterns with varying horizontal wavelengths in different x_0^* scenarios for larger $T = 6$ h. In contrast to the $T = 2$ h scenario, the horizontal wavelength is still primarily determined by the heating depth when $x_0^* = 50$ km (Figs. 10c,d). However, as x_0^* is further increased to 300 km, the horizontal wavelength also becomes less dependent on the vertical scale of heating and is mainly determined by the heating horizontal scale (Figs. 10e,f).

Authenticated duyu7@mail.sysu.edu.cn | Downloaded 07/31/24 01:46 AM UTC

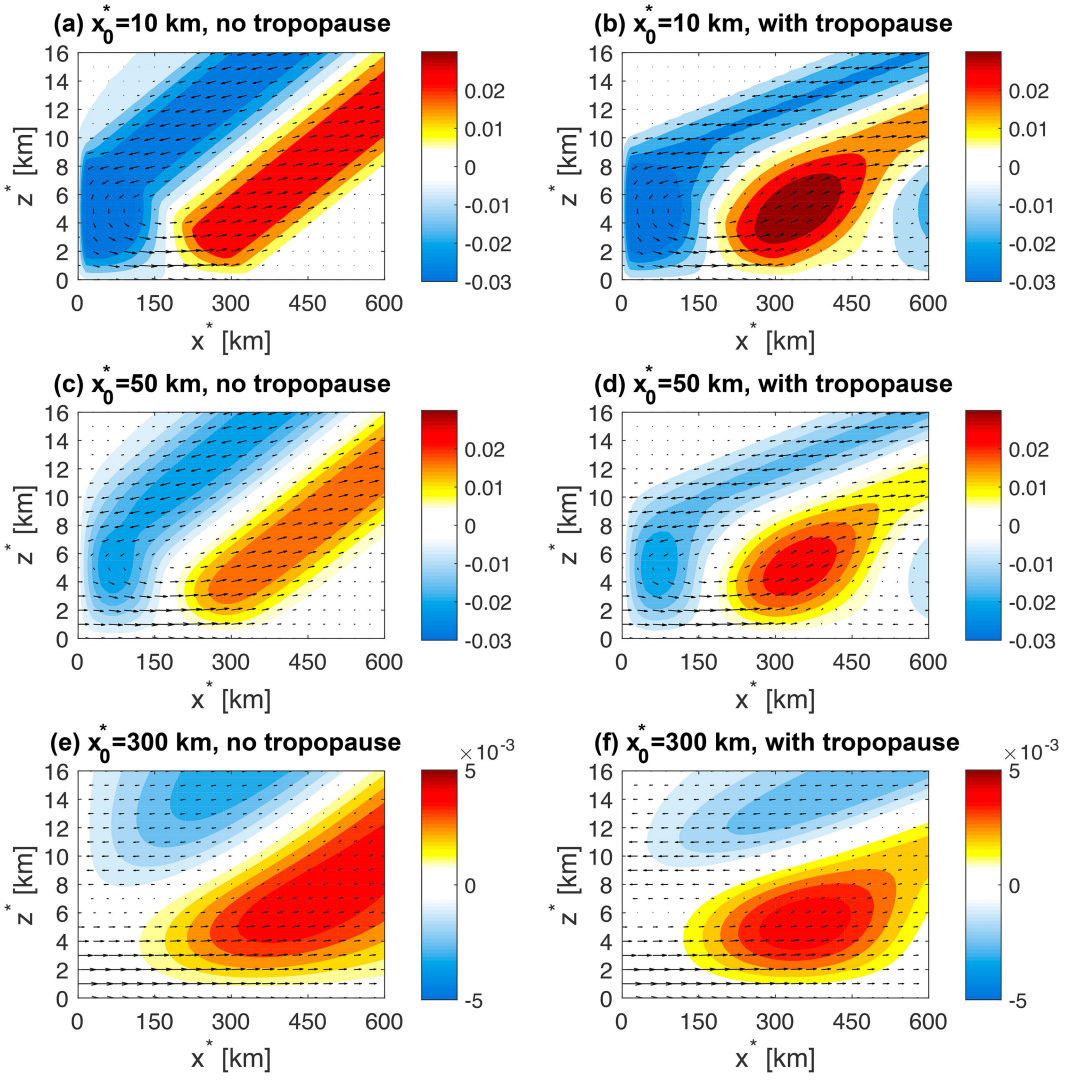

FIG. 10. The vertical cross section of vertical velocity (color shaded; m s^{-1}) and wind vectors (u^* and 10 w^*) forced by $n = 1$ mode convective heating with period $T = 6$ h and horizontal scale of (a),(b) 10; (c),(d) 50; and (e),(f) 300 km.

From a theoretical standpoint, we can further elaborate on this phenomenon. The integrand of (34) reduces to the expression

$$I \equiv \frac{Ke^{-x_0K}}{(n\pi)^2+\gamma^2}\frac{\sinh(\gamma)}{\gamma e^{-\gamma}} = \frac{Ke^{-x_0K}}{(n\pi)^2-\dfrac{N^2}{\sigma_r^2}K^2}\frac{\sinh(\gamma)}{\gamma e^{-\gamma}},$$

where $\gamma \cong i\sqrt{|(N^2-\sigma_r^2)/(f^2-\sigma_r^2)|K^2} \cong \pm i(N/\sigma_r)K$ when $f = 0$, $\alpha \to 0$, and $N_1 = N_2 = N \gg \sigma_r$. This expression can then be written as follows:

$$|I| \propto \left|\frac{Ke^{-x_0K}}{\left(\dfrac{n\pi\sigma_r}{N}\right)^2-K^2}\right|\left|\frac{\sin\left(\dfrac{N}{\sigma_r}K\right)}{\dfrac{N}{\sigma_r}K}\right| \propto \left|\frac{e^{-x_0K}}{\left(\dfrac{n\pi\sigma_r}{N}\right)^2-K^2}\right|\left|\sin\left(\frac{N}{\sigma_r}K\right)\right|.$$

Letting $n = 1$ and putting this formula into dimensional form gives

$$|I| \propto \left|\frac{e^{-x_0^*K^*}}{\left(\dfrac{\pi\sigma_r^*}{N^*H}\right)^2-K^{*2}}\right|\left|\sin\left(\frac{N^*H}{\sigma_r^*}K^*\right)\right| \propto \left|\frac{e^{-x_0^*[\sigma_r^*/(N^*H)]\kappa}}{\pi^2-\kappa^2}\right||\sin(\kappa)|,$$

where $\kappa = (N^*H/\sigma_r^*)K^*$. There are two limits of interest here:

1) When $x_0^*[\sigma_r^*/(N^*H)] \ll 1$, $|I| \propto |\sin(\kappa)/(\pi^2-\kappa^2)|$. The maximum of $|I|$ is at $\kappa \cong 2.631$ or $K^* \cong 2.3\times10^{-5}\text{m}^{-1}$ as in Figs. 8a and 8c. The term $|1/(\pi^2-\kappa^2)|$ is the effect of the periodic forcing; the term $|\sin(\kappa)|$ represents the wave vertical structure, which is unconstrained in the vertical without a tropopause. The peak $|I|$ occurs at κ where the forcing and wave structure are optimally superimposed.
2) When $x_0^*[\sigma_r^*/(N^*H)] \sim 1$, the exponential factor $e^{-x_0^*[\sigma_r^*/(N^*H)]\kappa}$ (the effect of the heating gradient) accounts for the shift

Authenticated duyu7@mail.sysu.edu.cn | Downloaded 07/31/24 01:46 AM UTC

of the peak to lower K^* for larger x_0^* as in Fig. 8e. As σ_r^* becomes smaller, $x_0^*[\sigma_r^*/(N^*H)]$ decreases, necessitating a larger x_0^* to ensure $x_0^*[\sigma_r^*/(N^*H)] \sim 1$ (Fig. 10e).

Note that in the case of a rigid lid ($N_1 \ll N_2$), $\gamma_1 S \to \gamma_1(N_2/2N_1)[\exp(-\gamma_1) - \exp(\gamma_1)] = -(N_2/N_1)\gamma_1 \sinh(\gamma_1) = -\gamma_2 \sinh(\gamma_1)$ in (31) so that

$$|I| \propto \left|\frac{1}{\pi^2 - \kappa^2}\right|,$$

and the peak $|I|$ should be at $\kappa = \pm\pi$, which gives $K^* \cong 2.7 \times 10^{-5}\,\mathrm{m}^{-1}$, as in Figs. 8b, 8d, 8f.

b. The period of convective heating

The evolution of convection involves diverse periods and frequencies. For instance, convective cells typically have lifetimes of 1–2 h, whereas mesoscale convective systems often last for 4–6 h. Furthermore, over land, convection exhibits an evident diurnal variation, with peak activity during the afternoon, corresponding to a 24-h cycle. In this study, we analyze the response of convective heating across periods of 2, 6, and 24 h.

Figure 11 visually demonstrates the similarity in horizontal and vertical structures of gravity waves but over larger horizontal domains for longer periods. Specifically, the horizontal wavelengths for $T = 24$ h and $T = 6$ h are 12 and 3 times larger, respectively, compared to the horizontal wavelength for $T = 2$ h. This result is consistent with the dispersion relationship $\lambda_x = Tc = TN^*H/(n\pi)$, indicating gravity waves characterized by lower frequencies (larger T) can propagate horizontally over more extensive distances. Previous studies have shown that gravity waves generated from individual convection typically affect regions within approximately 100 km of the source (Fovell et al. 2006; Yang et al. 2023). In contrast, diurnal gravity waves driven by land convection during the afternoon can exert influence over areas situated as far as ~1000 km offshore (Fang and Du 2022).

c. The background winds

Previous studies have extensively investigated the impact of background winds on the gravity waves resulting from the diurnal thermal contrast between land and sea (Qian et al. 2009; Du and Rotunno 2018; Du et al. 2019). Song and Chun (2005) solved the gravity wave spectrum in response to convection moving with a mean flow. Nevertheless, the specific influence of background winds on wave propagation behaviors generated by convection remains uncertain.

Figure 12 provides a comparative analysis of the $n = 1$ gravity wave response under varying background wind conditions. Above the tropopause, we observe a more pronounced inclination of phase lines relative to the vertical in the presence of $U^* = 10\,\mathrm{m\,s^{-1}}$ (Fig. 12b) in contrast to the scenario with no background wind (Fig. 12a), owing to the Doppler-shifting effect (Du and Rotunno 2018; Du et al. 2019). Additionally, below the tropopause, the presence of a background wind yields an expanded horizontal wavelength (~250 km for $U^* = 10\,\mathrm{m\,s^{-1}}$ compared to ~200 km for $U^* = 0\,\mathrm{m\,s^{-1}}$). The foregoing results suggest that background wind can extend the downstream propagation distance of gravity waves, consistent with findings by Du (2023).

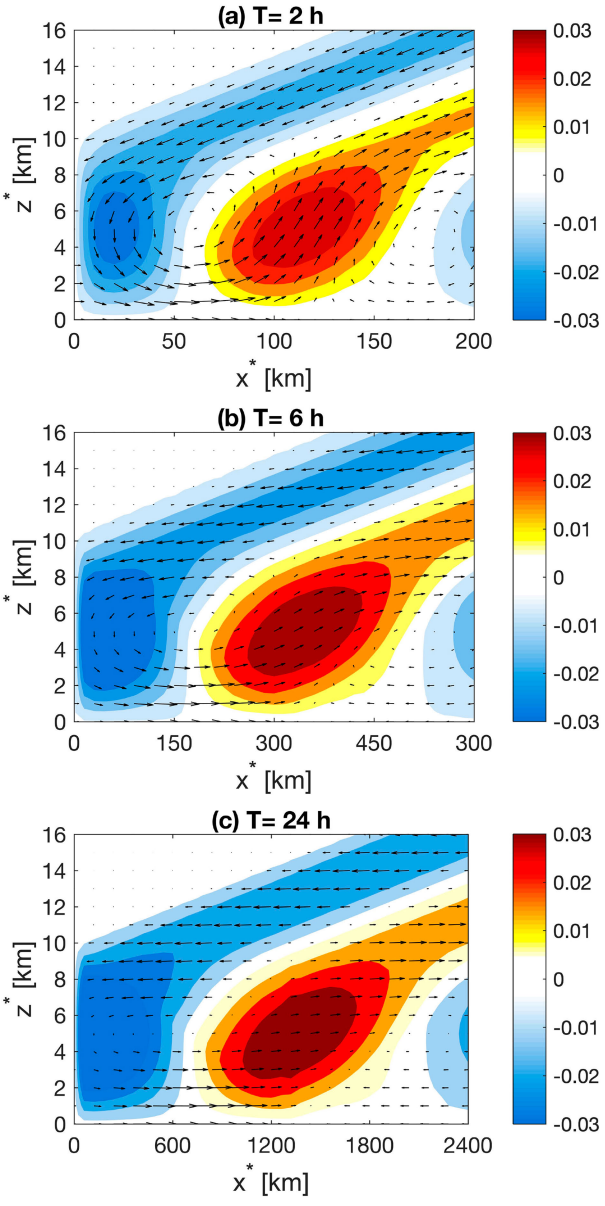

FIG. 11. As in Fig. 4b, but for (a) $T = 2$ h, (b) $T = 6$ h, and (c) $T = 24$ h. Note that the x^* axes cover a different range for each panel.

However, at larger background wind speed of 40 m s^{-1}, a significant transformation occurs in the gravity wave dynamics, characterized by negatively inclined phase lines both above and below the tropopause (Fig. 12c). Previous studies (Qian et al. 2009; Du and Rotunno 2018) have underscored that larger background wind amplifies a downstream-propagating wave mode with negative phase tilting, signifying that the phase lines tilt upstream with increasing height, akin to the flow past a stationary heat source or topographic obstacle. Remarkably, under these circumstances, the variation in horizontal wavelength becomes complicated with significantly stronger background

Authenticated duyu7@mail.sysu.edu.cn | Downloaded 07/31/24 01:46 AM UTC

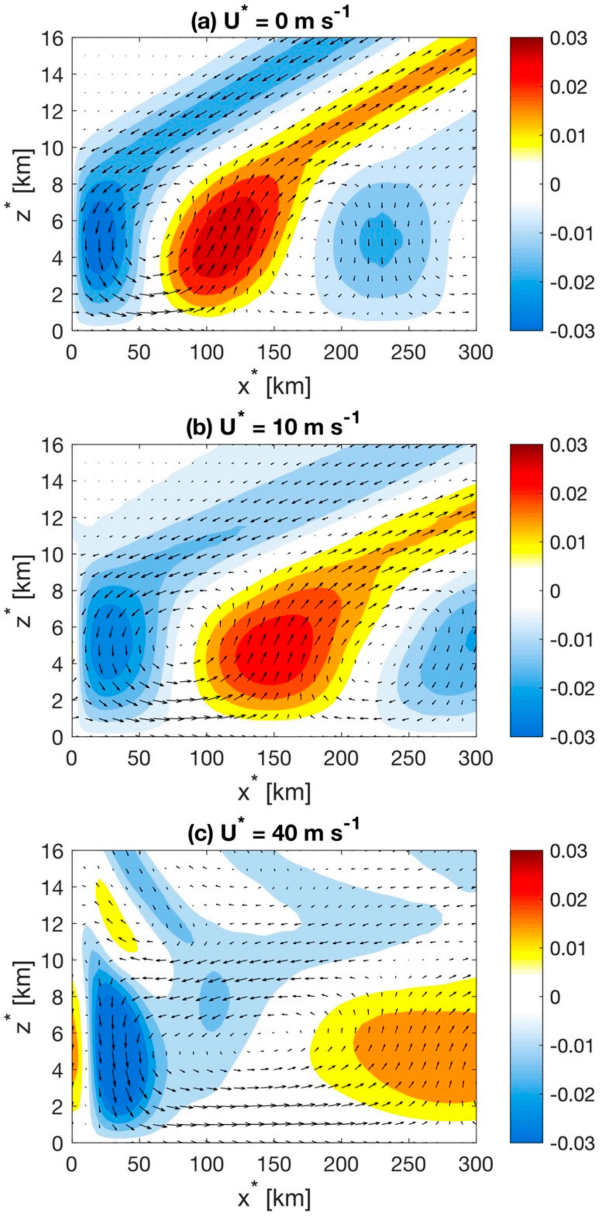

FIG. 12. As in Fig. 4b, but for (a) $U^* = 0\,\mathrm{m\,s^{-1}}$, (b) $U^* = 10\,\mathrm{m\,s^{-1}}$, and (c) $U^* = 40\,\mathrm{m\,s^{-1}}$.

wind as the preponderance of the dominant negative-tilted wave mode.

To understand the solution's dependence on background wind, we consider the parameter γ in (17)–(19). For $N^2 > \sigma_r^2 > f^2$ and $U = 0$, $\sigma_r = (1 - KU) = 1$ so that the parameter $\mathcal{B} > 0$ in (16) requires

$$\gamma \cong \sqrt{\left|\frac{\alpha\sigma_r N^2}{(f^2 - \sigma_r^2)^2}\right|K^2} + i\sqrt{\left|\frac{N^2 - \sigma_r^2}{f^2 - \sigma_r^2}\right|K^2}$$

from (17). The imaginary component of γ is positive and $e^{-i\sqrt{|(N^2-\sigma_r^2)/(f^2-\sigma_r^2)|K^2}z}$ represents the upward-propagating waves with positive tilting. Equation (31) has a singularity at $(\sigma^2 - f^2) = 0$. So $K = (1 - f)/U$. This dependence can help explain the phenomenon of increased horizontal wavelength (smaller K) due to higher background wind speed.

For nonzero U, note that $KU = k^*U^*/\omega$. For $U^* = 10\,\mathrm{m\,s^{-1}}$, Fig. 12b suggests $k^* \cong 2\pi/(300\,\mathrm{km}) = 2 \times 10^{-5}\mathrm{m^{-1}}$, and with $\omega = 2\pi/(7200\,\mathrm{s}) \cong 8.72 \times 10^{-4}\mathrm{s^{-1}}$, we have $\sigma_r = (1 - KU) = 1 - 0.023\,U^*$, which gives $\sigma_r > 0$ so that (17) still applies, and we expect positive tilting as shown in Fig. 12b.

For $U^* = 40\,\mathrm{m\,s^{-1}}$, Fig. 12c suggests $k^* \cong 2\pi/(100\,\mathrm{km}) = 6.28 \times 10^{-5}\mathrm{m^{-1}}$, $\sigma_r = (1 - KU) = -1.89 < 0$, and $N^2 > \sigma_r^2 > f^2$. The parameter $\mathcal{B} < 0$ in (16) requires

$$\gamma \cong \sqrt{\left|\frac{\alpha\sigma_r N^2}{(f^2 - \sigma_r^2)^2}\right|K^2} - i\sqrt{\left|\frac{N^2 - \sigma_r^2}{f^2 - \sigma_r^2}\right|K^2}.$$

The imaginary component of γ is negative, and $e^{\sqrt{|(N^2-\sigma_r^2)/(f^2-\sigma_r^2)|K^2}z}$ represents the upward-propagating waves with negative tilting (Du and Rotunno 2018), as shown in Fig. 12c. The real component is positive in both the foregoing cases, which allows that $e^{-\gamma z} < \infty$ for large z.

Therefore, background winds play a crucial role in shaping the attributes of convectively generated gravity waves, influencing their propagation behavior and phase tilts both above and below the tropopause.

d. *Latitudinal variations and the Coriolis force*

Previous discussions have omitted the consideration of the effect of Coriolis force. In this subsection, we explore the influence of latitude on the propagation of gravity waves generated by convection. For higher-frequency convection (e.g., $T = 2$ h, not shown), no discernible alteration in gravity wave response emerges across distinct latitudes. This consistent outcome can be attributed to the substantial discrepancy between the convection frequency $\omega = 2\pi/T$ and the Coriolis parameter $f = 2\Omega \sin\varphi$, where φ is the latitude and Ω is Earth's rotational angular velocity. Consequently, our primary exploration revolves around assessing the latitudinal dependency of gravity waves driven by diurnal convection.

Figure 13 illustrates the diverse responses across varying latitudes. At 20°N (Fig. 13b), the horizontal wavelength of gravity waves exceeds that at the equator (Fig. 13a) due to the dispersion relation $k^{*2} = [m^2(\omega^2 - f^2)]/N^{*2}$, where k^* represents the horizontal wavenumber and N^* is the Brunt–Väisälä frequency. This indicates that inertia–gravity waves can propagate over more extensive distances horizontally at higher latitudes when U and H are fixed between the latitudes. In contrast, at 40°N (beyond 30°N), the response takes on a trapped nature instead of gravity waves, attributed to the condition $\omega^2 - f^2 < 0$. These findings align with the distinctive responses of land–sea breeze at lower and higher latitudes (Rotunno 1983; Du and Rotunno 2015). In conclusion, the latitudinal dependence of gravity waves driven by diurnal convection is clearly discernible.

Authenticated duyu7@mail.sysu.edu.cn | Downloaded 07/31/24 01:46 AM UTC

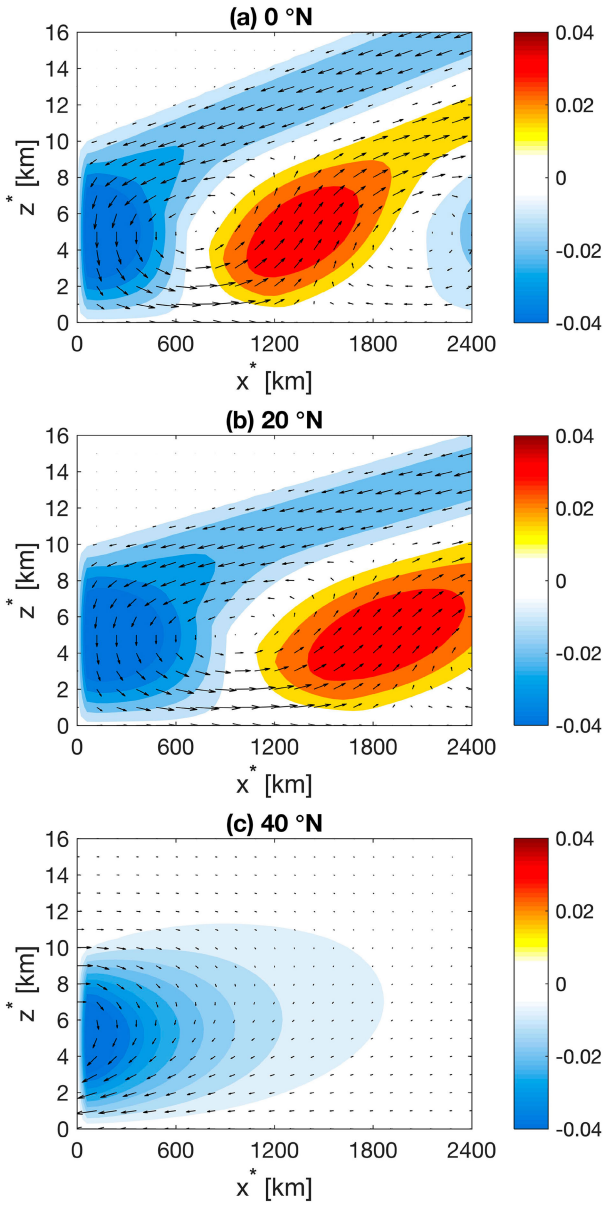

FIG. 13. As in Fig. 4b, but for $T = 24$ h at (a) 0°, (b) 20°N, and (c) 40°N.

We further examined the latitudinal dependence involving background winds. In Fig. 14a, the inertial gravity waves are emitted at 25°N in the absence of background wind, attributed to a frequency larger than the Coriolis frequency. Even with an increase in background wind to 4 m s^{-1}, the inertial gravity waves persist (Fig. 14b) as $(1 - KU)^2 - f^2$ remains greater than 0, despite a decrease in $(1 - KU)^2$. However, upon further increasing the background wind to 8 m s^{-1}, the response transits into a trapped nature instead of gravity waves (Fig. 14c) as $KU \to 1$, which implies $(1 - KU)^2 - f^2 < 0$. With a sufficiently large background wind, as $KU > 1$ and $(1 - KU)^2 - f^2 > 0$, the response of a downstream-propagating wave mode with negative phase tilting dominates (Fig. 14d).

5. Summary

In this study, we have developed a novel linear theory elucidating gravity waves generated by periodic convection near a coastline (arctangent-shaped source), offering a complement to prior linear frameworks centered on gravity waves triggered by constant or transient convective heating (Nicholls et al. 1991; Halliday et al. 2018). Our theoretical framework provides insights into the behavior and propagation characteristics of gravity waves associated with $n = 1$ deep convection or $n = 2$ stratiform heating/cooling. Additionally, we extensively explore the impacts of the various influential factors on gravity waves, including the horizontal length scale and period of convective heating, background wind, and latitude.

Far away from the heat source, free gravity waves featuring in-phase u and w are observed, whereas in the proximity of the heating source, a trapped-like manifestation of forced gravity waves becomes apparent, characterized by out-of-phase u and w. Notably, the presence of the tropopause facilitates an extended horizontal propagation range of forced gravity waves, achieved through reflective interaction between the surface and tropopause.

In the context of $n = 1$ gravity waves, vertical motion peaks at the middle level corresponding to the heating maximum, accompanied by a horizontal propagation speed of 31.9 m s^{-1} away from the convection source. On the other hand, $n = 2$ gravity waves exhibit opposing peaks at upper and lower levels aligned with heating and cooling maxima. The horizontal propagation speed of $n = 2$ waves is half that of $n = 1$ gravity waves due to the halved vertical scale of heating.

Significantly, the horizontal wavelength and propagation speed of gravity waves predominantly hinge upon the vertical scale of convective heating when the horizontal length scale of convective heating is small. Conversely, a larger horizontal length scale of convective heating has a substantial influence on the horizontal wavelength and propagation speed of the gravity waves produced.

Moreover, longer periods of convective heating extend the propagation distance of gravity waves away from the source. Background winds also increase the downstream propagation distance; however, gravity wave modes with negative tilts occur as the background wind strength is further enhanced.

Latitude emerges as a pivotal determinant in shaping the attributes of inertia–gravity waves generated by diurnal convection. At latitudes below 30°, higher latitudes enable inertia–gravity waves to propagate over longer horizontal distances, while latitudes greater than 30° lead to a horizontally trapped response for the same background wind and heating height.

A strong virtue of the analytical approach is that it allows one to understand the mathematical physics of the problem and also has value in that it is always correct up to the assumptions used (no finite difference approximations or other numerical errors). Our investigation provides insights into the intricate behavior and propagation dynamics of gravity waves generated through periodic convection. Understanding these

Authenticated duyu7@mail.sysu.edu.cn | Downloaded 07/31/24 01:46 AM UTC

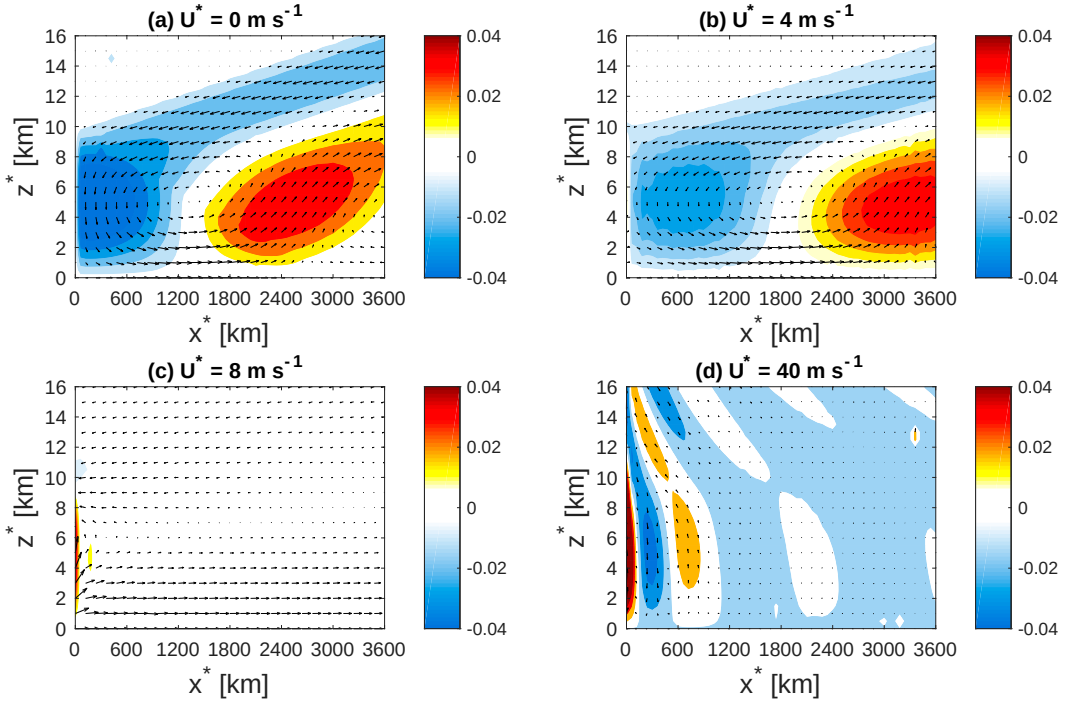

FIG. 14. As in Fig. 13a, but for (a) $U^* = 0\ \mathrm{m\ s^{-1}}$, (b) $U^* = 4\ \mathrm{m\ s^{-1}}$, (c) $U^* = 8\ \mathrm{m\ s^{-1}}$, and (d) $U^* = 40\ \mathrm{m\ s^{-1}}$ at 25°N.

dynamics enhances our knowledge of convectively generated gravity waves and their implications for weather and climate.

Acknowledgments. This study was supported by the National Natural Science Foundation of China (Grants 42122033 and 42075006), the Guangdong Major Project of Basic and Applied Basic Research (2020B0301030004), and the Key Innovation Team of China Meteorological Administration (CMA2023ZD08). We also acknowledge the high-performance computing support from School of Atmospheric Science of Sun Yat-sen University. Richard Rotunno is supported by the NSF National Center for Atmospheric Research, which is a major facility sponsored by the National Science Foundation under Cooperative Agreement 1852977.

Data availability statement. The model code and data in this study are available from the corresponding author upon request.

REFERENCES

Adams-Selin, R. D., 2020: Impact of convectively generated low-frequency gravity waves on evolution of mesoscale convective systems. *J. Atmos. Sci.*, **77**, 3441–3460, https://doi.org/10.1175/JAS-D-19-0250.1.

Alexander, M. J., J. R. Holton, and D. R. Durran, 1995: The gravity wave response above deep convection in a squall line simulation. *J. Atmos. Sci.*, **52**, 2212–2226, https://doi.org/10.1175/1520-0469(1995)052<2212:TGWRAD>2.0.CO;2.

Beres, J. H., 2004: Gravity wave generation by a three-dimensional thermal forcing. *J. Atmos. Sci.*, **61**, 1805–1815, https://doi.org/10.1175/1520-0469(2004)061<1805:GWGBAT>2.0.CO;2.

——, R. R. Garcia, B. A. Boville, and F. Sassi, 2005: Implementation of a gravity wave source spectrum parameterization dependent on the properties of convection in the Whole Atmosphere Community Climate Model (WACCM). *J. Geophys. Res.*, **110**, D10108, https://doi.org/10.1029/2004JD005504.

Du, Y., 2023: Offshore migration of summer monsoon low-level jet on a diurnal scale. *Geophys. Res. Lett.*, **50**, e2023GL103840, https://doi.org/10.1029/2023GL103840.

——, and R. Rotunno, 2015: Thermally driven diurnally periodic wind signals off the east coast of China. *J. Atmos. Sci.*, **72**, 2806–2821, https://doi.org/10.1175/JAS-D-14-0339.1.

——, and ——, 2018: Diurnal cycle of rainfall and winds near the south coast of China. *J. Atmos. Sci.*, **75**, 2065–2082, https://doi.org/10.1175/JAS-D-17-0397.1.

——, and F. Zhang, 2019: Banded convective activity associated with mesoscale gravity waves over southern China. *J. Geophys. Res. Atmos.*, **124**, 1912–1930, https://doi.org/10.1029/2018JD029523.

——, R. Rotunno, and F. Zhang, 2019: Impact of vertical wind shear on gravity wave propagation in the land–sea-breeze circulation at the equator. *J. Atmos. Sci.*, **76**, 3247–3265, https://doi.org/10.1175/JAS-D-19-0069.1.

Fang, J., and Y. Du, 2022: A global survey of diurnal offshore propagation of rainfall. *Nat. Commun.*, **13**, 7437, https://doi.org/10.1038/s41467-022-34842-0.

Fovell, R. G., G. L. Mullendore, and S.-H. Kim, 2006: Discrete propagation in numerically simulated nocturnal squall lines. *Mon. Wea. Rev.*, **134**, 3735–3752, https://doi.org/10.1175/MWR3268.1.

Fritts, D. C., and M. J. Alexander, 2003: Gravity wave dynamics and effects in the middle atmosphere. *Rev. Geophys.*, **41**, 1003, https://doi.org/10.1029/2001RG000106.

Authenticated duyu7@mail.sysu.edu.cn | Downloaded 07/31/24 01:46 AM UTC

Gallus, W. A., and R. H. Johnson, 1991: Heat and moisture budgets of an intense midlatitude squall line. *J. Atmos. Sci.*, **48**, 122–146, https://doi.org/10.1175/1520-0469(1991)048<0122:HAMBOA>2.0.CO;2.

Halliday, O. J., S. D. Griffiths, D. J. Parker, A. Stirling, and S. Vosper, 2018: Forced gravity waves and the tropospheric response to convection. *Quart. J. Roy. Meteor. Soc.*, **144**, 917–933, https://doi.org/10.1002/qj.3278.

Hassim, M. E. E., T. P. Lane, and W. W. Grabowski, 2016: The diurnal cycle of rainfall over New Guinea in convection-permitting WRF simulations. *Atmos. Chem. Phys.*, **16**, 161–175, https://doi.org/10.5194/acp-16-161-2016.

Houze, R. A., Jr., 1982: Cloud clusters and large-scale vertical motions in the tropics. *J. Meteor. Soc. Japan*, **60**, 396–410, https://doi.org/10.2151/jmsj1965.60.1_396.

Lane, T. P., 2015: Gravity waves: Convectively generated gravity waves. *Encyclopedia of Atmospheric Sciences*, Elsevier, 171–179.

——, and M. J. Reeder, 2001: Convectively generated gravity waves and their effect on the cloud environment. *J. Atmos. Sci.*, **58**, 2427–2440, https://doi.org/10.1175/1520-0469(2001)058<2427:CGGWAT>2.0.CO;2.

——, and F. Zhang, 2011: Coupling between gravity waves and tropical convection at mesoscales. *J. Atmos. Sci.*, **68**, 2582–2598, https://doi.org/10.1175/2011JAS3577.1.

Lindzen, R. S., and K.-K. Tung, 1976: Banded convective activity and ducted gravity waves. *Mon. Wea. Rev.*, **104**, 1602–1617, https://doi.org/10.1175/1520-0493(1976)104<1602:BCAADG>2.0.CO;2.

Love, B. S., A. J. Matthews, and G. M. S. Lister, 2011: The diurnal cycle of precipitation over the Maritime Continent in a high-resolution atmospheric model. *Quart. J. Roy. Meteor. Soc.*, **137**, 934–947, https://doi.org/10.1002/qj.809.

Nicholls, M. E., R. A. Pielke, and W. R. Cotton, 1991: Thermally forced gravity waves in an atmosphere at rest. *J. Atmos. Sci.*, **48**, 1869–1884, https://doi.org/10.1175/1520-0469(1991)048<1869:TFGWIA>2.0.CO;2.

Pandya, R., D. Durran, and C. Bretherton, 1993: Comments on "Thermally forced gravity waves in an atmosphere at rest". *J. Atmos. Sci.*, **50**, 4097–4101, https://doi.org/10.1175/1520-0469(1993)050<4097:COFGWI>2.0.CO;2.

Pandya, R. E., D. R. Durran, and M. L. Weisman, 2000: The influence of convective thermal forcing on the three-dimensional circulation around squall lines. *J. Atmos. Sci.*, **57**, 29–45, https://doi.org/10.1175/1520-0469(2000)057<0029:TIOCTF>2.0.CO;2.

Qian, T., C. C. Epifanio, and F. Zhang, 2009: Linear theory calculations for the sea breeze in a background wind: The equatorial case. *J. Atmos. Sci.*, **66**, 1749–1763, https://doi.org/10.1175/2008JAS2851.1.

Rotunno, R., 1983: On the linear theory of the land and sea breeze. *J. Atmos. Sci.*, **40**, 1999–2009, https://doi.org/10.1175/1520-0469(1983)040<1999:OTLTOT>2.0.CO;2.

Shige, S., and T. Satomura, 2001: Westward generation of eastward-moving tropical convective bands in TOGA COARE. *J. Atmos. Sci.*, **58**, 3724–3740, https://doi.org/10.1175/1520-0469(2001)058<3724:WGOEMT>2.0.CO;2.

Short, E., T. P. Lane, C. H. Bishop, and M. C. Wheeler, 2023: Diurnally forced tropical gravity waves under varying stability. *J. Atmos. Sci.*, **80**, 2557–2579, https://doi.org/10.1175/JAS-D-23-0074.1.

Song, I.-S., and H.-Y. Chun, 2005: Momentum flux spectrum of convectively forced internal gravity waves and its application to gravity wave drag parameterization. Part I: Theory. *J. Atmos. Sci.*, **62**, 107–124, https://doi.org/10.1175/JAS-3363.1.

——, ——, and T. P. Lane, 2003: Generation mechanisms of convectively forced internal gravity waves and their propagation to the stratosphere. *J. Atmos. Sci.*, **60**, 1960–1980, https://doi.org/10.1175/1520-0469(2003)060<1960:GMOCFI>2.0.CO;2.

——, ——, R. R. Garcia, and B. A. Boville, 2007: Momentum flux spectrum of convectively forced internal gravity waves and its application to gravity wave drag parameterization. Part II: Impacts in a GCM (WACCM). *J. Atmos. Sci.*, **64**, 2286–2308, https://doi.org/10.1175/JAS3954.1.

Stephan, C. C., N. Žagar, and T. G. Shepherd, 2021: Waves and coherent flows in the tropical atmosphere: New opportunities, old challenges. *Quart. J. Roy. Meteor. Soc.*, **147**, 2597–2624, https://doi.org/10.1002/qj.4109.

Su, T., and G. Zhai, 2017: The role of convectively generated gravity waves on convective initiation: A case study. *Mon. Wea. Rev.*, **145**, 335–359, https://doi.org/10.1175/MWR-D-16-0196.1.

Tulich, S. N., and B. E. Mapes, 2008: Multiscale convective wave disturbances in the tropics: Insights from a two-dimensional cloud-resolving model. *J. Atmos. Sci.*, **65**, 140–155, https://doi.org/10.1175/2007JAS2353.1.

Wilson, J. W., S. B. Trier, D. W. Reif, R. D. Roberts, and T. M. Weckwerth, 2018: Nocturnal elevated convection initiation of the PECAN 4 July hailstorm. *Mon. Wea. Rev.*, **146**, 243–262, https://doi.org/10.1175/MWR-D-17-0176.1.

Yang, H., and Y. Du, 2024: Difference between upshear- and downshear-propagating waves associated with the development of squall lines. *Mon. Wea. Rev.*, **152**, 1399–1420, https://doi.org/10.1175/MWR-D-23-0109.1.

——, ——, and J. Wei, 2023: Generation of multiple gravity wave couplets from convection. *J. Atmos. Sci.*, **80**, 2323–2343, https://doi.org/10.1175/JAS-D-22-0212.1.

Authenticated duyu7@mail.sysu.edu.cn | Downloaded 07/31/24 01:46 AM UTC